Planck intermediate results

II. Comparison of Sunyaev-Zeldovich measurements from *Planck* and from the Arcminute Microkelvin Imager for 11 galaxy clusters

Planck and AMI Collaborations: P. A. R. Ade[82], N. Aghanim[56], M. Arnaud[72], M. Ashdown[69,6], J. Aumont[56], C. Baccigalupi[81], A. Balbi[35], A. J. Banday[90,9], R. B. Barreiro[65], E. Battaner[92], R. Battye[68], K. Benabed[57,89], A. Benoît[54], J.-P. Bernard[9], M. Bersanelli[32,48], R. Bhatia[7], I. Bikmaev[20,3], H. Böhringer[77], A. Bonaldi[68], J. R. Bond[8], J. Borrill[14,85], F. R. Bouchet[57,89], H. Bourdin[35], M. L. Brown[68,⋆], M. Bucher[1], R. Burenin[83], C. Burigana[47,34], R. C. Butler[47], P. Cabella[36], P. Carvalho[6], A. Catalano[73,71], L. Cayón[29], A. Chamballu[52], R.-R. Chary[53], L.-Y. Chiang[61], G. Chon[77], D. L. Clements[52], S. Colafrancesco[44], S. Colombi[57,89], A. Coulais[71], B. P. Crill[67,79], F. Cuttaia[47], A. Da Silva[12], H. Dahle[63,11], R. D. Davies[68], R. J. Davis[68], P. de Bernardis[31], G. de Gasperis[35], A. de Rosa[47], G. de Zotti[43,81], J. Delabrouille[1], J. Démoclès[72], C. Dickinson[68], J. M. Diego[65], K. Dolag[91,76], H. Dole[56,55], S. Donzelli[48], O. Doré[67,10], M. Douspis[56], X. Dupac[40], G. Efstathiou[62], T. A. Enßlin[76], H. K. Eriksen[63], F. Feroz[6], F. Finelli[47], I. Flores-Cacho[9,90], O. Forni[90,9], P. Fosalba[58], M. Frailis[45], E. Franceschi[47], S. Fromenteau[1,56], S. Galeotta[45], K. Ganga[1], R. T. Génova-Santos[64], M. Giard[90,9], Y. Giraud-Héraud[1], J. González-Nuevo[65,81], K. M. Górski[67,94], K. J. B. Grainge[6,69], A. Gregorio[33,45], A. Gruppuso[47], F. K. Hansen[63], D. Harrison[62,69], S. Henrot-Versillé[70], C. Hernández-Monteagudo[13,76], D. Herranz[65], S. R. Hildebrandt[10], E. Hivon[57,89], M. Hobson[6], W. A. Holmes[67], K. M. Huffenberger[93], G. Hurier[73], N. Hurley-Walker[6], T. Jagemann[40], M. Juvela[25], E. Keihänen[25], I. Khamitov[88], R. Kneissl[39,7], J. Knoche[76], M. Kunz[18,56], H. Kurki-Suonio[25,42], G. Lagache[56], J.-M. Lamarre[71], A. Lasenby[6,69], C. R. Lawrence[67], M. Le Jeune[1], S. Leach[81], R. Leonardi[40], A. Liddle[24], P. B. Lilje[63,11], M. Linden-Vørnle[17], M. López-Caniego[65], G. Luzzi[70], J. F. Macías-Pérez[73], C. J. MacTavish[69], D. Maino[32,48], N. Mandolesi[47,5], M. Maris[45], F. Marleau[60], D. J. Marshall[72], E. Martínez-González[65], S. Masi[31], M. Massardi[46], S. Matarrese[30], F. Matthai[76], P. Mazzotta[35], P. R. Meinhold[27], A. Melchiorri[31,49], J.-B. Melin[16], L. Mendes[40], A. Mennella[32,48], S. Mitra[51,67], M.-A. Miville-Deschênes[56,8], L. Montier[90,9], G. Morgante[47], D. Munshi[82], P. Naselsky[78,37], P. Natoli[34,4,47], H. U. Nørgaard-Nielsen[17], F. Noviello[68], D. Novikov[52], I. Novikov[78], M. Olamaie[6], S. Osborne[87], F. Pajot[56], D. Paoletti[47], F. Pasian[45], G. Patanchon[1], T. J. Pearson[10,53], O. Perdereau[70], Y. C. Perrott[6], F. Perrotta[81], F. Piacentini[31], E. Pierpaoli[23], P. Platania[66], E. Pointecouteau[90,9], G. Polenta[4,44], L. Popa[59], T. Poutanen[42,25,2], G. W. Pratt[72], J.-L. Puget[56], J. P. Rachen[21,76], R. Rebolo[64,15,38], M. Reinecke[76], M. Remazeilles[56,1], C. Renault[73], S. Ricciardi[47], I. Ristorcelli[90,9], G. Rocha[67,10], C. Rodríguez-González[6], C. Rosset[1], M. Rossetti[32,48], J. A. Rubiño-Martín[64,38], C. Rumsey[6], B. Rusholme[53], M. Sandri[47], R. D. E. Saunders[6,69], G. Savini[80], M. P. Schammel[6], D. Scott[22], T. W. Shimwell[6], G. F. Smoot[26,75,1], J.-L. Starck[72], F. Stivoli[50], V. Stolyarov[6,69,86], R. Sudiwala[82], R. Sunyaev[76,84], D. Sutton[62,69], A.-S. Suur-Uski[25,42], J.-F. Sygnet[57], J. A. Tauber[41], L. Terenzi[47], L. Toffolatti[19,65], M. Tomasi[48], M. Tristram[70], L. Valenziano[47], B. Van Tent[74], P. Vielva[65], F. Villa[47], N. Vittorio[35], L. A. Wade[67], B. D. Wandelt[57,89,28], D. Yvon[16], A. Zacchei[45], and A. Zonca[27]

(Affiliations can be found after the references)

ABSTRACT

A comparison is presented of Sunyaev-Zeldovich measurements for 11 galaxy clusters as obtained by *Planck* and by the ground-based interferometer, the Arcminute Microkelvin Imager. Assuming a universal spherically-symmetric Generalised Navarro, Frenk and White (GNFW) model for the cluster gas pressure profile, we jointly constrain the integrated Compton-Y parameter (Y_{500}) and the scale radius (θ_{500}) of each cluster. Our resulting constraints in the $Y_{500} - \theta_{500}$ 2D parameter space derived from the two instruments overlap significantly for eight of the clusters, although, overall, there is a tendency for AMI to find the Sunyaev-Zeldovich signal to be smaller in angular size and fainter than *Planck*. Significant discrepancies exist for the three remaining clusters in the sample, namely A1413, A1914, and the newly-discovered *Planck* cluster PLCKESZ G139.59+24.18. The robustness of the analysis of both the *Planck* and AMI data is demonstrated through the use of detailed simulations, which also discount confusion from residual point (radio) sources and from diffuse astrophysical foregrounds as possible explanations for the discrepancies found. For a subset of our cluster sample, we have investigated the dependence of our results on the assumed pressure profile by repeating the analysis adopting the best-fitting GNFW profile shape which best matches X-ray observations. Adopting the best-fitting profile shape from the X-ray data does not, in general, resolve the discrepancies found in this subset of five clusters. Though based on a small sample, our results suggest that the adopted GNFW model may not be sufficiently flexible to describe clusters universally.

Key words. cosmology: observations – galaxies: clusters: general – galaxies: clusters: intracluster medium – cosmic background radiation – X-rays: galaxies: clusters

1. Introduction

Clusters of galaxies are the most massive gravitationally bound objects in the Universe and as such are critical tracers of the formation of large-scale structure. The size and formation history of massive clusters is such that the ratio of cluster gas mass to total mass is expected to be representative of the universal ratio, once the relatively small amount of baryonic matter in the cluster galaxies is taken into account (e.g., White et al. 1993). Moreover, the comoving number density of clusters as a function of mass and redshift is expected to be particularly sensitive to

---

⋆ Corresponding author: M. L. Brown,
e-mail: mbrown@jb.man.ac.uk

the cosmological parameters σ_8 and Ω_m (e.g., Battye & Weller 2003).

The Sunyaev-Zeldovich (SZ) effect (see Birkinshaw 1999; Carlstrom et al. 2002, for reviews) produces secondary anisotropies in the cosmic microwave background (CMB) radiation through inverse-Compton scattering from the electrons in the hot intracluster gas (which also radiates via thermal Bremsstrahlung in the X-ray waveband) and the transfer of some of the energy of the electrons to the low-energy photons. Moreover, the surface brightness of an SZ signal does not depend on the redshift z of the cluster. Hence an SZ-effect flux-density-limited survey can provide a complete catalogue of galaxy clusters above a limiting mass (e.g., Bartlett & Silk 1994; Kneissl et al. 2001; Kosowsky 2003; Ruhl et al. 2004).

Analyses of observations of galaxy clusters via their SZ effect, X-ray emission or gravitational lensing are often based on some spherically-symmetric cluster model in which one assumes parameterised functional forms for the radial distribution of some cluster properties, such as electron density and temperature (Sanderson et al. 2003; Vikhlinin et al. 2005, 2006; LaRoque et al. 2006; Feroz et al. 2009b; Zwart et al. 2011; Rodríguez-Gonzálvez et al. 2011; Hurley-Walker et al. 2011; Shimwell et al. 2012), electron pressure and density (Nagai et al. 2007; Mroczkowski et al. 2009; Arnaud et al. 2010; Plagge et al. 2010; Planck Collaboration 2011e), or electron pressure and entropy (Olamaie et al. 2010; Allison et al. 2011).

The motivation for this paper is to augment SZ measurements obtained with *Planck*[1] for a sample of 11 galaxy clusters with refined higher-resolution SZ measurements obtained with the Arcminute Microkelvin Imager (AMI) interferometer. Such a combination is an interesting and potentially very powerful way to pin down the gas pressure profile of individual galaxy clusters as it relies on a single well-understood astrophysical effect. In addition, *Planck* and AMI SZ measurements exploit very different aspects of the SZ signature: *Planck* effectively uses its wide frequency coverage to identify the characteristic frequency spectrum of the SZ effect while AMI exploits its higher angular resolution to perform spatial filtering to identify SZ clusters and constrain their parameters. Combining measurements by these two instruments not only provides a powerful consistency check on both sets of observations, but may also break, or at least reduce, the observed parameter degeneracy between the derived SZ Compton-Y parameter and the cluster angular size which often results due to the finite resolution of SZ telescopes (Planck Collaboration 2011e).

The paper is organised as follows. In Sect. 2, we outline how we selected our sample of 11 galaxy clusters for this comparison work. In Sects. 3 and 4, we describe the *Planck* and AMI observations of our cluster sample, respectively. In Sect. 5 we present the pressure profile that we have used to model the clusters and constrain parameters. The analysis of the real data from both experiments is also described in Sect. 5. We follow this by validating our analysis methodology and investigating the effects of diffuse foreground emission on the *Planck* constraints with simulations in Sect. 6.1. Section 6.2 presents a similar simulations-based investigation of the effects of residual point sources and analysis methodology on the constraints derived from the AMI

interferometric data. With a view to explaining some of the discrepancies we observe, in Sect. 7, we investigate the possibility of relaxing the assumptions regarding the universal pressure profile adopted for our cluster sample. Here we also examine the consistency of the *Planck* and AMI SZ results with complementary constraints from high-quality X-ray observations for a subset of our cluster sample. We conclude with a discussion in Sect. 8.

2. Selection of the cluster sample

An original sample of 26 clusters was defined at the beginning of this study. 24 of the clusters were identified as members of the sample by virtue of the fact that they were both present in the *Planck* Early Sunyaev-Zeldovich (ESZ) cluster catalogue (Planck Collaboration 2011e), and had also already been observed and detected with AMI during the course of its normal observing programme. Note that these 24 clusters had been observed by AMI as part of differing scientific programmes and while each programme had a well-defined sample, the resulting set of clusters used in this paper does not constitute a well-defined or complete sample.

To this sample of 24, two newly-discovered *Planck* clusters were added, for which AMI made follow-up observations. The complete list of the original cluster sample, their coordinates and redshifts is presented in Table 1. The sample was then screened to include only clusters that had (i) a firm SZ detection by AMI ($\geq 3\sigma$ before source subtraction and $\geq 5\sigma$ after source subtraction); and (ii) a benign environment in terms of radio point sources. For the purposes of this screening process, we define a "benign environment" as a cluster field in which both (i) the total (summed) flux density from all detected point sources within $3'$ of the cluster centre is less than 5 mJy; and (ii) the total flux density from all point sources detected within $10'$ of the cluster centre is less than 10 mJy. Note that we define a "detection" to be a positive signal with flux density $>3.5\sigma_{LA}$ where σ_{LA} is the thermal noise on the LA map. Typically, $\sigma_{LA} \approx 0.10$ mJy beam^{-1} over the majority of the LA maps with deeper observations reaching $\sigma_{LA} \approx 0.03$ mJy beam^{-1} towards the cluster centres in each case. This reduced the sample to 11 clusters spanning a wide range in redshift, $0.11 < z < 0.55$. The clusters in the new sample are A2034, A1413, A990, A2409, A1914, A2218, A773, MACS J1149+2223, RXJ0748+5941, PLCKESZ G139.59+24.18, and PLCKESZ G121.11+57.01. The sample includes two cool-core clusters, A1413 and A2034 (Pratt & Arnaud 2002; Kempner et al. 2003; Vikhlinin et al. 2005; Govoni et al. 2009) and two newly-discovered *Planck* clusters, PLCKESZ G139.59+24.18 and PLCKESZ G121.11+57.01 (Planck Collaboration 2011e). The last two have been observed in the optical with the Russian-Turkish 1.5 m Telescope (RTT-150)[2] as part of the *Planck* follow-up programme. The resulting spectroscopic redshifts measured for the brightest cluster galaxies within these two clusters are also given in Table 1.

3. Description of *Planck* data

Planck (Tauber et al. 2010; Planck Collaboration 2011a) is the third generation space mission to measure the anisotropy of the CMB. It observes the sky in nine frequency bands covering 30–857 GHz with high sensitivity and angular resolution from $31'$ to $5'$. The Low Frequency Instrument (LFI; Mandolesi et al. 2010; Bersanelli et al. 2010; Mennella et al. 2011) covers the

---

[1] *Planck* (http://www.esa.int/Planck) is a project of the European Space Agency (ESA) with instruments provided by two scientific consortia funded by ESA member states (in particular the lead countries France and Italy), with contributions form NASA (USA) and telescope reflectors provided by a collaboration between ESA and a scientific consortium led and funded by Denmark.

[2] http://hea.iki.rssi.ru/rtt150/en/

Table 1. Original sample of 26 clusters.

ESZ cluster name	Alternative cluster name	Right ascension (J2000)	Declination (J2000)	RA and Dec reference	Redshift	Redshift reference	Rejection reason
PLCKESZ G139.59+24.18	⋯	06:21:58.00	+74:42:15.7	8	0.27	9	in sample
PLCKESZ G167.65+17.64	ZwCl 0634.1+4750	06:38:04.00	+47:47:53.0	1, 7	0.17	1, 7	i
PLCKESZ G056.80+36.30	MACS J0717.5+3745	07:17:30.93	+37:45:29.7	6	0.55	6	ii-b
PLCKESZ G157.43+30.33	RXJ0748+5941	07:48:45.60	+59:41:41.0	2	0.55	2	in sample
PLCKESZ G149.70+34.70	A665	08:30:58.50	+65:51:03.7	3	0.18	3	ii-b
PLCKESZ G186.40+37.30	A697	08:42:57.56	+36:21:59.3	3	0.28	3	ii-b
PLCKESZ G166.13+43.39	A773	09:17:52.97	+51:43:55.5	3	0.22	3	in sample
PLCKESZ G195.60+44.10	A781	09:20:26.08	+30:30:54.0	3	0.30	3	ii-a
PLCKESZ G163.70+53.50	A980	10:22:28.10	+50:07:15.6	3	0.16	3	ii-b
PLCKESZ G165.08+54.11	A990	10:23:41.83	+49:08:38.2	3	0.14	3	in sample
PLCKESZ G228.15+75.19	MACS J1149+2223	11:49:34.30	+22:23:42.5	6	0.55	6	in sample
PLCKESZ G226.24+76.76	A1413	11:55:18.24	+23:24:28.6	3	0.14	3	in sample
PLCKESZ G180.60+76.70	A1423	11:57:22.10	+33:37:55.2	3	0.21	3	i
PLCKESZ G229.60+78.00	A1443	12:01:17.00	+23:06:18.0	4	0.27	4	ii-a, b
PLCKESZ G125.70+53.90	A1576	12:36:58.96	+63:11:26.5	3	0.30	3	ii-a
PLCKESZ G121.11+57.01	⋯	12:59:23.80	+60:05:24.8	8	0.34	9	in sample
PLCKESZ G118.40+39.30	RXCJ1354.6+7715	13:54:37.80	+77:15:34.6	4	0.40	4	i
PLCKESZ G067.23+67.46	A1914	14:26:02.15	+37:50:05.8	3	0.17	3	in sample
PLCKESZ G053.52+59.54	A2034	15:10:10.80	+33:30:21.6	3	0.11	3	in sample
PLCKESZ G044.20+48.70	A2142	15:58:22.10	+27:13:58.8	3	0.09	3	ii-b
PLCKESZ G097.73+38.11	A2218	16:35:52.80	+66:12:50.0	3	0.17	3	in sample
PLCKESZ G086.50+15.30	A2219	16:40:22.56	+46:42:32.4	3	0.23	3	ii-a, b
PLCKESZ G056.80+36.30	A2244	17:02:42.87	+34:03:42.8	3	0.10	3	ii-a
PLCKESZ G055.60+31.90	A2261	17:22:27.09	+32:08:01.7	3	0.22	3	ii-a, b
PLCKESZ G086.50+15.30	CIZA J1938.3+5409	19:38:18.60	+54:09:33.0	5	0.26	5	i
PLCKESZ G077.90−26.64	A2409	22:00:53.03	+20:57:38.3	3	0.15	3	in sample

Notes. The meaning of the notes in the right-most column are: (i) cluster has SZ detection smaller than 3σ before source subtraction and smaller than 5σ after source subtraction; (ii-a) cluster has a total integrated source flux density greater than 5 mJy within a radius of 3′; (ii-b) cluster has a total integrated source flux density greater than 10 mJy within a radius of 10′. "in sample" indicates that the cluster is included in the 11-cluster sample analysed in this paper.

References. For cluster information: (1) Crawford et al. (1995); (2) Appenzeller et al. (1998); (3) Ebeling et al. (1998); (4) Böhringer et al. (2000); (5) Ebeling et al. (2002); (6) Ebeling et al. (2007); (7) Kocevski et al. (2007); (8) Planck Collaboration (2011e); and (9) *Planck* RTT follow-up programme; see Sect. 2.

30, 44, and 70 GHz bands with amplifiers cooled to 20 K. The High Frequency Instrument (HFI; Lamarre et al. 2010; Planck HFI Core Team 2011a) covers the 100, 143, 217, 353, 545, and 857 GHz bands with bolometers cooled to 0.1 K. Polarisation is measured in all but the highest two bands (Leahy et al. 2010; Rosset et al. 2010). A combination of radiative cooling and three mechanical coolers produces the temperatures needed for the detectors and optics (Planck Collaboration 2011b). Two data processing centers (DPCs) check and calibrate the data and make maps of the sky (Planck HFI Core Team 2011b; Zacchei et al. 2011). *Planck*'s sensitivity, angular resolution, and frequency coverage make it a powerful instrument for Galactic and extragalactic astrophysics as well as cosmology. Early astrophysics results are given in Planck Collaboration 2011d–v, based on data taken between 13 August 2009 and 7 June 2010. Intermediate astrophysics results are now being presented in a series of papers based on data taken between 13 August 2009 and 27 November 2010.

We note that the *Planck* maps used for the analysis in this paper are not the same as those used in the Early *Planck* results papers. In particular, we stress that both the data and the analysis techniques employed for this study are not the same as was used to construct the *Planck* ESZ catalogue (Planck Collaboration 2011e). A later version of the data has been used for the analysis here and we use different analysis techniques for reasons which will be explained in Sect. 5.1. However, as part of our suite of internal tests, we have repeated our analysis on the older version

of the *Planck* data which was used to derive the ESZ catalogue and we find excellent agreement.

In Fig. 1 we present maps of the dimensionless Compton-y parameter for each of the clusters as estimated from the *Planck* data. The y-parameter is related to the observed brightness as a function of frequency (ν) by

$$\frac{\Delta T_{tSZ}}{T_{CMB}}(\nu) = y \cdot g(\nu), \tag{1}$$

where ΔT_{tSZ} is the brightness fluctuation due to the thermal SZ (tSZ) effect and T_{CMB} is the temperature of the CMB, which we take to be 2.7255 ± 0.0006 (Fixsen 2009). The function, $g(\nu)$ is the frequency dependence of the SZ effect (Sunyaev & Zeldovich 1972). For the HFI channel frequencies (100, 143, 217, 353, 545 and 857 GHz), $g(\nu)$ takes the values $(-4.03, -2.78, 0.19, 6.19, 14.47$ and 26.36 $K_{CMB}/y)$. The maps of Fig. 1 were estimated from HFI channel data taken between 13 August 2009 and 27 November 2010, corresponding to slightly more than 2.5 full-sky scans. The measured noise levels on the *Planck* frequency channel maps are listed in Table 2 (Planck HFI Core Team, in prep.). The tSZ signal reconstructions were performed using the MILCA method (Hurier et al. 2010 and references therein) on the six *Planck* all-sky maps from 100 GHz to 857 GHz. MILCA (Modified Internal Linear Combination Algorithm) is a component separation approach aimed at extracting a chosen component (here the tSZ signal) from a multi-channel set of input maps. It is based on the well
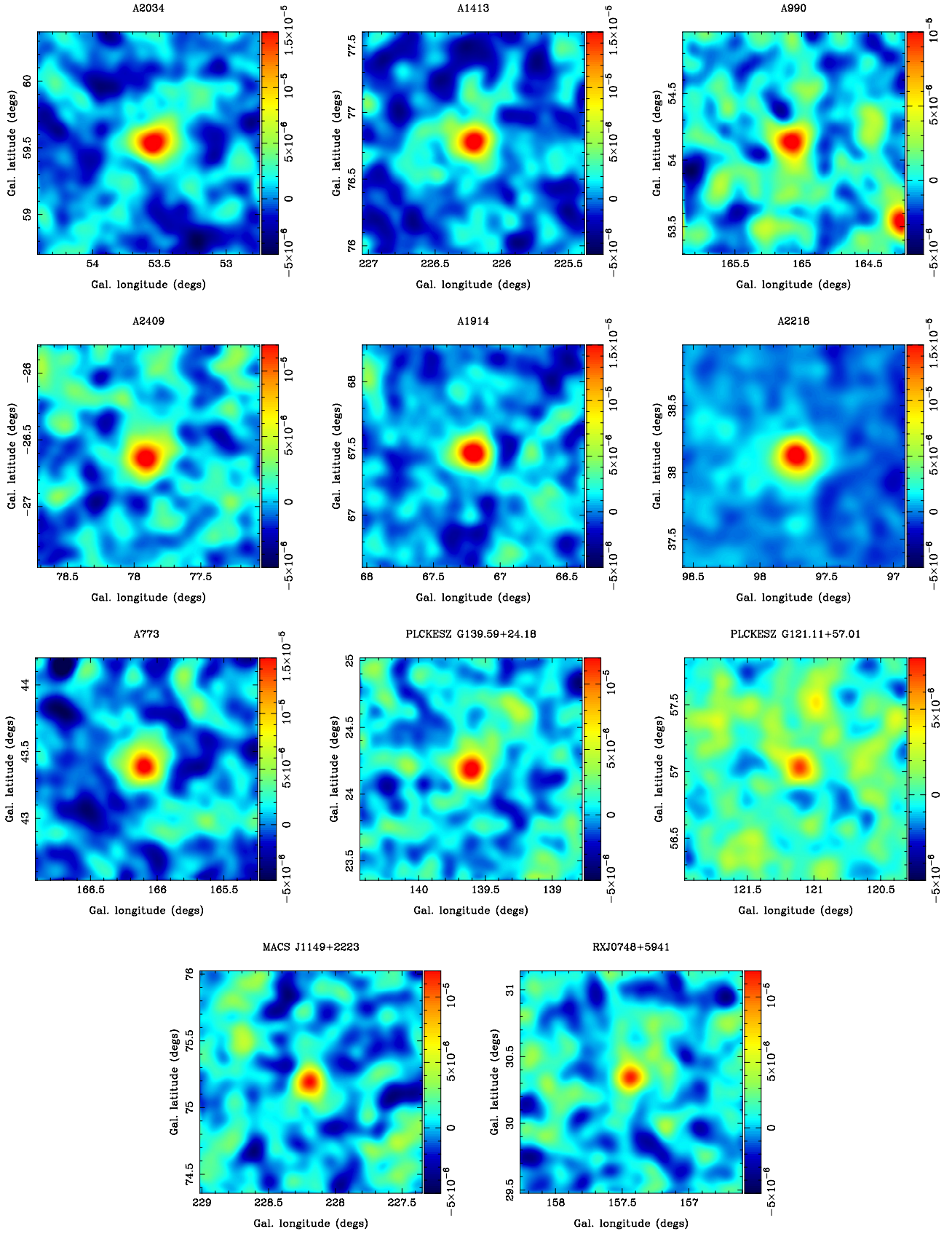
Fig. 1. Maps of the dimensionless Compton-y parameter (Eq. (1)) as estimated from the *Planck* observations using the MILCA algorithm. The maps have an effective resolution of 10 arcmin. The clusters are ordered in terms of increasing redshift, from *top left to bottom right*. Each panel shows a $100' \times 100'$ region.

Table 2. Noise levels per N_{side} = 2048 pixel for each *Planck* frequency band.

Freq. (GHz)	100	143	217	353	545	857
Noise (μK)	80	34	56	167	1414	170 200

Table 3. Assumed $I + Q$ flux densities of 3C286 and 3C48 over the commonly-used AMI band, and FWHM of the LA primary beam (approximate field of view, Θ_{LA}) for each channel.

Channel	ν/GHz	S^{3C286}/Jy	S^{3C48}/Jy	Θ_{LA}/ arcmin
3	13.9	3.74	1.89	6.08
4	14.6	3.60	1.78	5.89
5	15.3	3.47	1.68	5.70
6	16.1	3.35	1.60	5.53
7	16.9	3.24	1.52	5.39
8	17.6	3.14	1.45	5.25

known ILC approach (e.g., Eriksen et al. 2004), which searches for the linear combination of the input maps that minimises the variance of the final reconstructed map, while imposing spectral constraints. Hurier et al. (2010) present tests of the performance of MILCA in terms of its ability to reconstruct SZ cluster signals from Planck-like simulations and the algorithm has subequently been used to reconstruct SZ maps from *Planck* data in a number of previous publications (Planck Collaboration 2011e,i, 2012). For our cluster SZ reconstructions, we applied MILCA using two constraints, the first one to preserve the tSZ signal and the second one to remove CMB contamination in the final tSZ *y*-map. In addition, to compute the weights of the linear combination, we have used the extra degrees of freedom to minimise residuals from other components (two degrees) and from the noise (two degrees). The noise covariance matrix was estimated from jack-knife maps. The final *y*-maps have an effective resolution of 10 arcmin. Note that, in general, the properties of the foreground emission depend on both the position on the sky and on the frequency of observation. We have therefore allowed the weights to vary as a function of both position and frequency. We have confirmed using simulations that such an approach maximises the signal-to-noise and minimises the bias in the extraction of the tSZ signal. We emphasise that the MILCA SZ reconstructions presented in Fig. 1 are intended for visual examination and qualitative assessment of the cluster signals only. Our quantitative analysis of the *Planck* data, which we use to compare with the AMI results, is based mainly on the PowellSnakes (Carvalho et al. 2012) SZ extraction algorithm (see Sect. 5).

4. Description of AMI data

AMI comprises two arrays, the Small Array (SA) and the Large Array (LA), located at the Mullard Radio Astronomy Observatory near Cambridge. The SA consists of ten 3.7-m diameter equatorially-mounted antennas, with a baseline range of $\simeq$5–20 m and synthesised beam (resolution) of around 3′. The LA consists of eight 13-m diameter antennas with a baseline range of $\simeq$20–100 m and synthesised beam of around 30″. Both arrays observe Stokes $I + Q$ in the band 13–18 GHz, each with system temperatures of about 25 K. Note that AMI defines Stokes Q and U with respect to celestial north. The backends are analogue Fourier transform spectrometers, from which the complex signals in each of eight channels of 750-MHz bandwidth are synthesised, and the signals in the adjacent channels are correlated at the $\simeq$10% level. Further details of the instrument are given in Zwart et al. (2008).

SA pointed observations of our cluster sample were taken during 2007–2011. The observation lengths per cluster before any flagging of the data are presented in Table 4; the noise levels on the SA maps reflect the actual observation time used. The SA observations were made with single pointings interspersed with a phase calibration source, while full-field LA observations were made in a 61+19-point raster mode configuration with 4′ spacing. This consisted of 61 pointings arranged in a hexagonal grid, with grid points separated by 4′ with further observations

of the central 19 pointings designed to increase the sensitivity at the centre of the field. In this mode the integration time on the area $\leq$7.5′ from the cluster centre is twice as long as the area >7.5′ away, so as to provide a better match to the primary beam sensitivity of the AMI SA. In addition to the 61+19-point raster coverage of the entire field, very deep single pointings were conducted with the LA towards the centre of each cluster in order to search for a possible over-density of faint radio sources associated with the clusters themselves. Phase calibrators were chosen from the Jodrell Bank VLA Astrometric Survey (JVAS, Patnaik et al. 1992) on the basis of proximity ($\leq$2° for the AMI LA, $\leq$8° for the AMI SA) and 15 GHz flux density ($\geq$0.2 Jy for the AMI LA, $\geq$0.7 Jy for the AMI SA). The JVAS is based on observations made with the VLA in "A" configuration (Condon & Broderick 1985, 1986; Condon et al. 1989; White & Becker 1992).

The reduction of the AMI data was performed using a dedicated software tool REDUCE. This is used to apply path-compensator and path-delay corrections, to flag interference, shadowing and hardware errors, to apply phase and amplitude calibrations and to Fourier transform the correlator data readout to synthesise the frequency channels, before outputting to disc.

Flux calibration was performed using short observations of 3C 48 and 3C 286 near the beginning and end of each run. The assumed $I + Q$ flux densities for these sources in the AMI channels are listed in Table 3 and are consistent with Baars et al. (1977). As Baars et al. measure I and AMI measures $I + Q$, these flux densities include corrections for the polarisation of the sources. An amplitude correction is also made for the intervening air mass during the observation. Flux calibration is expected to be accurate to $\simeq$3% for the AMI SA and $\simeq$5% for the AMI LA. After phase calibration, the phase of both arrays over one hour is generally stable to 5° for channels 4–7, and to 10° for channels 3 and 8. (Channels 1 and 2 are generally not used for science analysis as they tend to suffer from interference problems).

Maps were made using the Astronomical Image Processing System (AIPS, Greisen 2003) from each channel of the AMI SA and LA; however here we present only the combined-channel maps of the SA and LA observations. The AIPS task imean was used on the LA individual maps to attach the map noise to the map header. imean fits a Gaussian to the histogram of the map pixels (ignoring extreme pixels that might be due to sources) and uses the standard deviation of the fitted Gaussian as a measure of the random noise in the data. The AIPS task flatn was then used to form a mosaiced image from the multiple pointings. Data from the pointings were primary beam corrected using parameters listed in Table 3 and weighted accordingly when combined. The AMI SA combined-channel map noise and the LA map noise are given in Table 5. The raw *uv* data for all good observations were concatenated together to make a visibility data file for

Table 4. Details of the AMI observations of our cluster sample.

| Cluster	Observing dates	SA observing time (h)	LA observing time (h)	SA phase calibrator	LA phase calibrator
A2034	2010 Jan., Mar., Dec.; 2012 July	38	31	J1506+3730	J1504+3249
A1413	2007 Mar., Nov.; 2010 Mar.; 2012 July	40	27	J1159+2914	J1150+2417
A990	2007 Feb., Nov; 2009 Apr.; 2012 July	31	25	J0958+4725	J1015+4926
A2409	2007 Mar., Apr., May; 2009 Dec.; 2012 July	38	29	J2225+2118	J2200+2137
A1914	2008 May, 2009 Jan., Jun.; 2012 July	32	43	J1419+3821	J1419+3821
A2218	2008 Jan.; 2009 Feb., Jun.; 2012 July	30	20	J1642+6856	J1623+6624
A773	2007 Sep., Oct.; 2009 May; 2012 July	40	27	J0903+4651	J0929+5013
MACS J1149+2223	2010 Apr., May, Nov., Dec.; 2012 July	38	19	J1150+2417	J1150+2417
RXJ0748+5941	2011 Feb.; 2012 July	45	43	J0753+5352	J0737+5941
PLCKESZ G139.59+24.18	2010 Nov.; 2012 July	52	45	J0639+7324	J0639+7324
PLCKESZ G121.11+57.01	2011 Jan.; 2012 July	40	75	J1302+5748	J1302+5748

Table 5. Details of radio point sources and the thermal noise levels for the AMI observations of the cluster sample.

A	B	C	D	E	F	G
A2034	13	32.5	0.08	0.08	0.025	10
A1413	21	47.7	0.09	0.12	0.023	12
A990	20	56.3	0.11	0.10	0.029	8
A2409	14	49.2	0.11	0.10	0.032	11
A1914	15	31.8	0.12	0.10	0.032	11
A2218	10	31.9	0.11	0.15	0.031	12
A773	9	13.6	0.12	0.12	0.033	6
MACS J1149+2223	15	45.2	0.09	0.14	0.028	17
RXJ0748+5941	15	17.1	0.07	0.06	0.025	12
PLCKESZ G139.59+24.18	14	13.2	0.09	0.06	0.028	11
PLCKESZ G121.11+57.01	19	25.4	0.07	0.06	0.035	10

Notes. Columns are: (A) Cluster name; (B) number of LA sources detected at $S/N \geq 3.5\sigma_{LA}$; (C) total source flux (mJy beam^{-1}); (D) σ_{SA} (mJy beam^{-1}); (E) σ_{LA} (mJy beam^{-1}); (F) σ_{LA} (mJy beam^{-1}) for deep LA pointings towards cluster centres (see description of AMI data in Sect. 4); and (G) S/N of SZ decrement detection. σ_{SA} and σ_{LA} refer to the thermal noise levels reached in the LA and SA maps. S/N is calculated by dividing the peak flux values by σ_{SA}.

each channel. All maps were made using natural *uv* weighting and all images were CLEANED to three times the thermal noise with a single clean box encompassing the entire map. The data were also binned into bins of width 40λ. This reduced the size of the data to a manageable level without adversely affecting the subsequent inference of cluster properties. Figure 2 shows a typical example of the SA synthesised beam, in this case for the observations of A2218.

As contamination from radio sources at 16 GHz tends to be significant, removing or modelling this emission accurately can often be essential to recover SZ decrements from AMI maps. To address this issue, we use the AMI-developed source extraction software, SOURCEFIND (Waldram et al. 2003; Franzen et al. 2011) to determine the position, flux density and spectral index of the radio sources with flux density $\geq 3.5\sigma_{LA}$ on the CLEANED LA continuum maps, where σ_{LA} is the LA thermal noise. Spectral indices were fit with a Markov Chain Monte Carlo (MCMC) method using LA maps for all six channels and assuming that source flux densities follow a power-law relation of $S \propto \nu^{-\alpha}$ for the AMI frequencies. These source parameter estimates are subsequently used as priors in our Bayesian analysis of the cluster SZ signals (Sect. 5.2). Tables 4 and 5 summarise the observational details of our cluster sample and Figs. 3 and 4 present the maps of the AMI observations of these clusters before and after source subtraction, respectively. Once again, as with the reconstructed *Planck* maps presented in the previous section, the AMI maps presented in
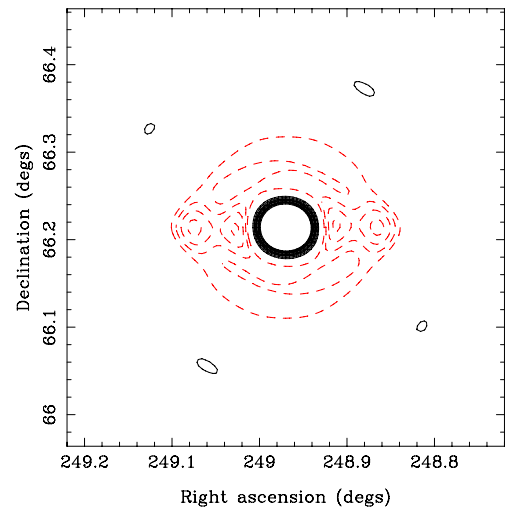

Fig. 2. SA synthesised beam for the A2218 observations. Contours start at 6% and increase linearly by 3% per contour. Contours drawn as red dashed lines are negative. The synthesised beams for the other cluster observations are qualitatively similar.

Figs. 3 and 4 are intended for visual examination and qualitative assessment of the cluster signals only. Our quantitative analysis of the AMI data is described later in Sect. 5.2.
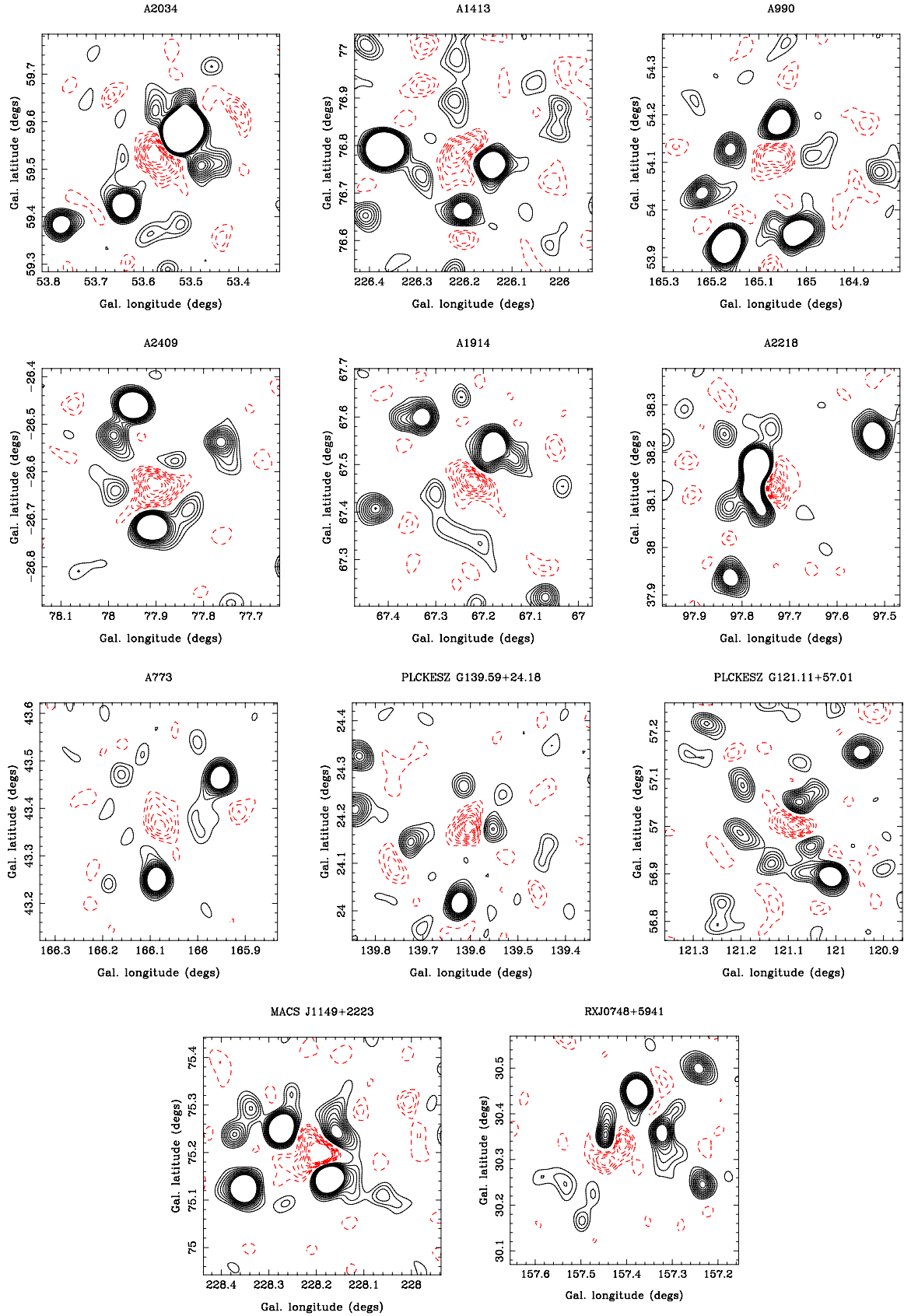
Fig. 3. AMI 16 GHz flux density maps before source subtraction. The clusters are ordered as in Fig. 1, in terms of increasing redshift. Black solid lines represent positive contours and red dashed lines indicate negative contours. The contours increase linearly from $\pm 2\sigma_{\mathrm{SA}}$ to $\pm 10\sigma_{\mathrm{SA}}$ where σ_{SA} is listed in Table 5 for each cluster. Each map covers a region approximately $30' \times 30'$ and the resolution is around $3'$.
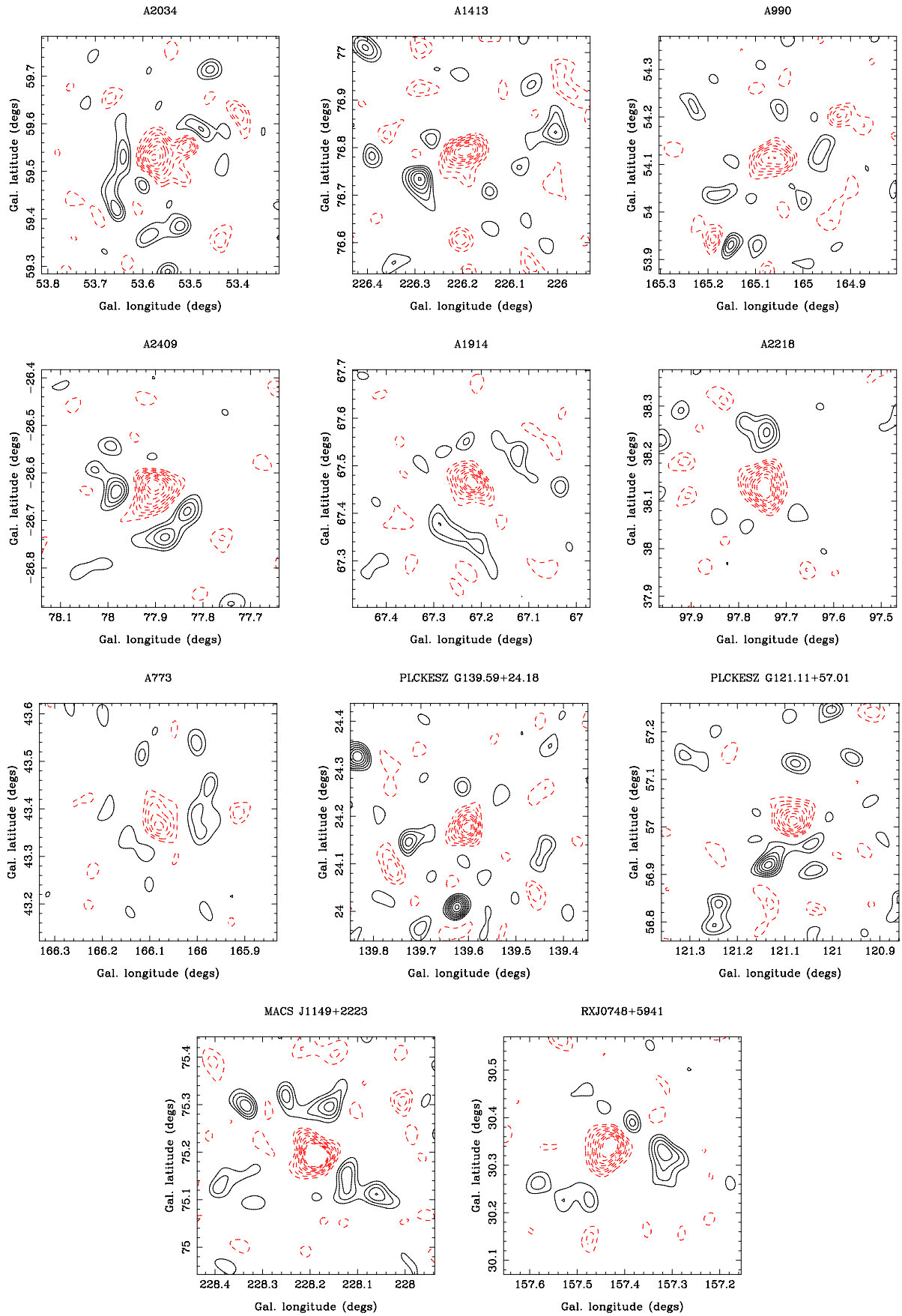
Fig. 4. AMI 16 GHz flux density maps after subtraction of radio point sources. The solid black lines represent positive contours and the dashed red lines indicate negative contours. The cluster ordering, contour levels and resolution are the same as in Fig. 3.

5. Analysing the SZ signal

The SZ surface brightness (the Compton-y parameter, cf., Eq. (1)) is proportional to the line of sight integral of the electron pressure,

$$y = \frac{\sigma_{\text{T}}}{m_{\text{e}}c^2} \int_{-\infty}^{+\infty} P_{\text{e}}(r)\text{d}l, \tag{2}$$

where $P_{\text{e}}(r)$ is the electron pressure at radius r, σ_{T} is the Thomson scattering cross-section, m_{e} is the electron mass, c is the speed of light and $\text{d}l$ is the line element along the line of sight. In this context, Nagai et al. (2007) analysed the pressure profiles of a series of simulated clusters (Kravtsov et al. 2005) as well as a sample of relaxed real clusters presented in Vikhlinin et al. (2005, 2006). They found that the pressure profiles of all of these clusters could be described by a generalisation of the Navarro, Frenk, and White (NFW, Navarro et al. 1997) model used to describe the dark matter halos of simulated clusters. Assuming spherical geometry, the GNFW pressure profile (Nagai et al. 2007) reads

$$P_{\text{e}}(r) = P_0 \left(\frac{r}{r_{\text{s}}}\right)^{-\gamma} \left[1 + \left(\frac{r}{r_{\text{s}}}\right)^{\alpha}\right]^{(\gamma-\beta)/\alpha}, \tag{3}$$

where P_0 is the overall normalisation coefficient of the pressure profile and r_{s} is the scale radius. It is common to define the latter in terms of r_{500}, the radius at which the mean density is 500 times the critical density at the cluster redshift, and to define the gas concentration parameter, $c_{500} = r_{500}/r_{\text{s}}$. The parameters (α, β, γ) describe the slopes of the pressure profile at $r \simeq r_{\text{s}}$, $r > r_{\text{s}}$, and $r \ll r_{\text{s}}$ respectively. In order to retain consistency between the *Planck* and AMI analysis pipelines, we follow (Arnaud et al. 2010, see also Planck Collaboration 2011e,f) and fix the values of the gas concentration parameter and the slopes to be $(c_{500}, \alpha, \beta, \gamma) = (1.156, 1.0620, 5.4807, 0.3292)$. These values describe the "universal pressure profile", derived from *XMM-Newton* observations of the REXCESS cluster sample (Böhringer et al. 2007), and from three different sets of detailed numerical simulations by Borgani et al. (2004), Piffaretti & Valdarnini (2008), and Nagai et al. (2007), which take into account radiative cooling, star formation, and energy feedback from supernova explosions. In Sect. 7, we will relax these restrictions for a subset of our cluster sample and will include information from X-ray observations of individual clusters in our analysis. We note that the profile of Eq. (3) has recently been used to analyse SZ data from the South Pole Telescope (SPT, Plagge et al. 2010) in addition to the *Planck* survey data (Planck Collaboration 2011e,f).

The integral of the y parameter over the solid angle Ω subtended by the cluster is denoted by Y_{SZ}, and is proportional to the volume integral of the gas pressure. It is thus a good indicator of the total thermal energy content of the cluster and its mass (e.g., Bartlett & Silk 1994). The determination of the normalisation and the slope of the $Y_{\text{SZ}} - M$ relation has therefore been a major goal of studies of the SZ effect (da Silva et al. 2004; Nagai 2006; Kravtsov et al. 2006; Plagge et al. 2010; Arnaud et al. 2010; Andersson et al. 2011; Planck Collaboration 2011e,c,f,g,h). In particular, Andersson et al. (2011) investigated the $Y_{\text{SZ}} - Y_{\text{X}}$ scaling relation within a sample of 15 clusters observed by SPT, *Chandra* and *XMM-Newton* and found a slope of close to unity (0.96 ± 0.18). Similar studies were carried out by Planck Collaboration (2011g) using a sample of 62 nearby ($z < 0.5$) clusters observed by both *Planck* and by *XMM-Newton*. The results are consistent with predictions from X-ray studies

(Arnaud et al. 2010; Andersson et al. 2011). These studies at low redshifts, where data are available from both X-ray and SZ observations of galaxy clusters, are crucial to calibrate the $Y_{\text{SZ}} - M$ relation, as such a relation can then be scaled and used to determine masses of SZ selected clusters at high redshifts in order to constrain cosmology.

The integrated y parameter (Y_{SZ}) adopting a spherical geometry Y_{sph}, is given by

$$Y_{\text{sph}}(r) = \frac{\sigma_{\text{T}}}{m_{\text{e}}c^2} \int_0^r P_{\text{e}}(r')4\pi r'^2 \text{d}r'. \tag{4}$$

Following Arnaud et al. (2010), we consider the radius of $5r_{500}$ as the boundary of the cluster where the pressure profile flattens, and we use this boundary to define the total volume integrated SZ signal, Y_{tot}.

In the simplest case, where α, β, γ, and c_{500} in Eq. (3) have fixed values, our cluster model depends only on four parameters: x_{c} and y_{c} which define the projected cluster position on the sky and P_0 and r_{s} in the pressure profile (Eq. (3)). In this paper, we define clusters in terms of the parameter set $\mathbf{\Theta}_{\text{c}} \equiv (x_{\text{c}}, y_{\text{c}}, \theta_{\text{s}} = r_{\text{s}}/D_{\text{A}}, Y_\theta = Y_{\text{tot}}/D_{\text{A}}^2)$, where D_{A} is the angular-diameter distance to the cluster (Planck Collaboration 2011e), and we determine the model parameter P_0 by evaluating Eq. (4) at $r = 5r_{500}$. To calculate D_{A} we assume a flat Universe with matter density $\Omega_{\text{m}} = 0.27$ and Hubble constant $H_0 = 70.4 \text{ km s}^{-1} \text{ Mpc}^{-1}$ (Komatsu et al. 2011).

We adopt an exponential prior for θ_{s} and a power-law prior for Y_θ to analyse both the *Planck* and AMI data (Carvalho et al. 2012). The prior on θ_{s} is $\lambda e^{-\lambda\theta_{\text{s}}}$ for $1.3' < \theta_{\text{s}} < 45'$ and zero outside this range, with $\lambda = 0.2$. The prior on Y_θ is $Y_\theta^{-\alpha}$ for $5.0 \times 10^{-4} \text{ arcmin}^2 < Y_\theta < 0.2 \text{ arcmin}^2$ and zero outside this range, with $\alpha = 1.6$. These priors have already been used in *Planck* detection and extraction algorithms to identify and characterise compact objects buried in a diffuse background (Planck Collaboration 2011e). For the cluster position, however, in order to ensure that we are comparing integrated SZ fluxes centred on identical positions on the sky, we performed an initial analysis of the AMI data using a Gaussian prior centred on the cluster phase centre and with a standard deviation of $1'$ in order to find the best-fitting cluster coordinates. We then fixed the cluster position to these best-fitting coordinates in the subsequent analysis of the *Planck* data and also in a subsequent reanalysis of the AMI data.

5.1. Analysis of Planck data

The analysis of the *Planck* data was performed using POWELLSNAKES (PwS), which is a Bayesian package for discrete object detection, photometry and astrometry, as described in Carvalho et al. (2009, 2012). PwS is part of the *Planck* HFI pipeline and is regularly used to produce catalogues of objects (Planck Collaboration 2011d) and to measure and characterise the SZ signal (Planck Collaboration 2011e). Note that we have chosen to use PwS as our primary SZ extraction algorithm for the *Planck* analysis in this study as PwS naturally returns the full posterior distribution in the $Y_{500} - \theta_{500}$ 2D parameter space. It is thus naturally suited for combining with the AMI results to produce joint constraints. We will also present a comparison with results obtained using the Matched Multi-Filter algorithm (MMF3; Melin et al. 2006) which was the reference algorithm adopted for the production of the *Planck* ESZ catalogue (Planck Collaboration 2011e). However, in its current

implementation, the MMF3 algorithm does not produce any information on the correlation between the two cluster parameters of interest (Y_{500} and θ_{500}) and so producing joint constraints as obtained from AMI and *Planck* via MMF3 is currently not possible.

The analysis of the *Planck* data using the PwS algorithm proceeded as follows. For each cluster, flat patches ($14.7° \times 14.7°$; 512×512 pixels) were created using a gnomonic projection, centred on the targeted cluster, for each of the *Planck* HFI channels. By operating on such a large patch of sky enough statistics are collected in order to produce a smooth cross-channel covariance matrix. The position of each cluster was assumed to be known precisely (we adopted delta-function priors at the AMI-determined position) as described in Sect. 5.

The data model for a single isolated cluster located in the centre of the patch is then described by

$$d(x) = Y f \Gamma(\theta_s, x) + n(x), \qquad (5)$$

where x is sky position, $d(x)$ is a vector containing the data, $n(x)$ is the background composed of instrumental noise plus all other astronomical components except the SZ signal, f is a vector containing the SZ surface brightness at each frequency, Y is the total integrated Comptonisation parameter, θ_s is a parameter controlling the cluster radial scale and $\Gamma(\theta_s, x)$ is the convolution of the canonical GNFW model integrated along the line of sight with the *Planck* beam at that channel. It is assumed that the background is a realisation of a stationary Gaussian random field.

A direct computation of the likelihood is very expensive. Therefore, PwS instead computes the likelihood ratio of two competing models describing the data: a cluster is present (H_1); or no cluster is present (H_0). Note that the latter hypothesis does not contain any parameters and therefore only multiplies the target likelihood in H_1 by a constant. The representation of the likelihood ratio in real space reads

$$
\ln\left[\frac{\mathcal{L}_H(\Theta)}{\mathcal{L}_{H_0}(\Theta)}\right] = Y\mathcal{F}^{-1}\left[\mathcal{P}_j(\eta)\widetilde{\tau}(-\eta;\theta_s)\right]_{x=0} \\
- \frac{1}{2}Y^2\sum_\eta Q_{jj}(\eta)|\widetilde{\tau}(\eta;\theta_s)|^2, \qquad (6)
$$

where η is the spatial frequency (the conjugate variable to x) and $\mathcal{F}^{-1}[\ldots]_x$ denotes the inverse Fourier transform of the quantity in brackets, evaluated at the point x. We have also defined the quantities $\mathcal{P}_j(\eta) \equiv \widetilde{d}^t(\eta)N^{-1}(\eta)\psi(\eta)$ and $Q_{ij}(\eta) \equiv \widetilde{\psi}_i^t(\eta)N^{-1}(\eta)\psi_j(\eta)$, in which the vector $\psi_i(\eta)$ has the components $(\psi_i)_\nu = \widetilde{B}_\nu(\eta)(f_i)_\nu$, with ν labelling frequency channels and $\widetilde{B}_\nu(\eta)$ is the beam transfer function. The quantity $\widetilde{\tau}(-\eta;\theta_s)$ is the Fourier transform of $\Gamma(\theta_s, x)$ and the matrix $N(\eta)$ contains the generalised noise cross-power spectra. We refer the interested reader to Carvalho et al. (2009, 2012) for further technical details on the PwS algorithm.

The cross-channel covariance matrix is computed directly from the pixel data, by averaging the Fourier modes in concentric annuli. This operation is only possible because of the assumed isotropy of the background. To reduce the contamination of the background by the signal itself, the estimation of the covariance matrix is performed iteratively. After an initial estimate, all detected clusters in the patch are subtracted from the data using their best fit values and the covariance matrix is re-estimated. To enforce our assumption of a single source in the centre of the patch, PwS removes from the data all other detections with S/Ns

higher than our target cluster to reduce possible contamination of the signal by power leakage from nearby objects. Bright point sources are masked or subtracted from the maps as part of a preprocessing routine run prior to the production of the flat patches.

To construct the joint posterior distributions of (Y, θ_s), we have used the set of priors as described in Sect. 5. To draw the posterior distribution manifold, PwS grids the parameter space using a uniformly spaced lattice of (256×256) cells, appropriately chosen to enclose all posterior regions significantly different from zero.

Since the LFI channels of *Planck* have relatively coarse resolution, the use of LFI bands in current implementations of the extraction algorithms results in beam dilution of the SZ signal and thus decreases the S/N for the detected clusters (Planck Collaboration 2011e). This can potentially be improved in the future with modifications to the algorithms but for the purposes of the present study, we use only the HFI data.

5.2. Analysis of AMI data

An interferometer like AMI operating at a frequency ν measures samples from the complex visibility plane $\tilde{I}_\nu(u)$. These are given by a weighted Fourier transform of the surface brightness $I_\nu(x)$, namely

$$\tilde{I}_\nu(u) = \int A_\nu(x)I_\nu(x)\exp(2\pi i u \cdot x)\mathrm{d}x, \qquad (7)$$

where x is the position relative to the phase centre, $A_\nu(x)$ is the (power) primary beam of the antennas at observing frequency ν (normalised to unity at its peak) and u is the baseline vector in units of wavelength. In our model, the measured visibilities are defined as

$$V_\nu(u) = S_\nu(u) + N_\nu(u), \qquad (8)$$

where the signal component, $S_\nu(u)$, contains the contributions from the SZ cluster and identified radio point sources, whereas the generalised noise part, $N_\nu(u)$, contains contributions from a background of unsubtracted radio point sources, primary CMB anisotropies and instrumental noise.

We assume a Gaussian distribution for the generalised noise. This then defines the likelihood function for the data

$$\mathcal{L}(\Theta) = \frac{1}{Z_N}\exp\left(-\frac{1}{2}\chi^2\right), \qquad (9)$$

where χ^2 is the standard statistic quantifying the misfit between the observed data D and the predicted data $D^p(\Theta)$,

$$\chi^2 = \sum_{\nu,\nu'}(D_\nu - D_\nu^p)^T(C_{\nu,\nu'})^{-1}\left(D_{\nu'} - D_{\nu'}^p\right), \qquad (10)$$

where ν and ν' are channel frequencies. Here C is the generalised noise covariance matrix

$$C = C_{\nu,\nu'}^{\mathrm{rec}} + C_{\nu,\nu'}^{\mathrm{CMB}} + C_{\nu,\nu'}^{\mathrm{conf}}. \qquad (11)$$

The first term on the right hand side of Eq. (11) is a diagonal matrix with elements $\sigma_{\nu,i}^2 \delta_{ij}\delta_{\nu\nu'}$, where $\sigma_{\nu,i}$ is the rms Johnson (receiver) noise on the ith element of the data vector D_ν at frequency ν. The second term denotes the noise due to primordial CMB anisotropies and contains significant off-diagonal elements, both between visibility positions and between frequencies. This term can be calculated from a given primary CMB power spectrum $C_l^{\mathrm{CMB}}(\nu)$ following

Hobson & Maisinger (2002); note that in intensity units the CMB power spectrum is a function of frequency. To calculate this term, we adopt the best-fitting CMB power spectrum to the *WMAP* 7-year data (Komatsu et al. 2011). The third term on the right hand side of Eq. (11) is the source confusion noise, which accounts for remaining unresolved radio sources with flux densities less than the flux limit (S_{lim}) of the AMI observations and which remain after high resolution observation and subtraction. We estimate this term assuming that sources are randomly distributed on the sky, in which case we can describe the source confusion noise with a power spectrum calculated as

$$C_\ell^{\text{conf}}(\nu) = \int_0^{S_{\text{lim}}} S^2 n_\nu(S)\, dS, \tag{12}$$

where $n_\nu(S) = dN_\nu(>S)/dS$ is the differential source count at frequency ν as a function of flux density S. We use the source counts as measured by the 10C survey (Davies et al. 2011) for our calculation. The limiting flux density for the integration (S_{lim}) is determined from the noise in the LA maps and is different for each cluster, but is typically in the range 0.2–0.5 mJy.

The normalisation factor Z_N in Eq. (9) is given by

$$Z_N = (2\pi)^{(2N_{\text{vis}})/2}|C|^{1/2}, \tag{13}$$

where N_{vis} is the total number of visibilities. Further details on our Bayesian methodology, generalised noise model, likelihood function and resolved radio point-source models are given in Feroz & Hobson (2008) and Feroz et al. (2009a,b).

Radio sources detected in the LA maps were modeled by four source parameters, $\Theta_s \equiv (x_s, y_s, S_0, \alpha)$, where x_s and y_s refer to the right ascension and declination of radio sources, respectively, while S_0 and α are the flux density and spectral index of the radio source at the central frequency, ν_0. As mentioned in Sect. 4, this modelling is necessary because of source variability and some difficulty with inter-array calibration. Therefore, the properties of point sources detected at >$3.5\,\sigma_{\text{LA}}$ by the LA (in both the 61+19 raster observations as well as in the deep central pointings; see Sect. 4) were used as priors when modelling the SA data. We used a delta-function prior on the position of the source since the resolution of the LA is around three times that of the SA. We used Gaussian priors on the source flux densities, with LA (integrated, where applicable) flux densities generating the peak of the prior, and the Gaussian σs were set to 40% of the source flux densities. Spectral index (α) priors were also set as Gaussians, with σ equal to the error on the spectral index fit. This is because for sources with high signal-to-noise ratio (S/N), the determination of the spectral index is dominated by the AMI frequency channel mean and the error on α is Gaussian. For sources with low S/N which just meet our continuum detection threshold, the spectral index probability distribution is dominated by the prior, which is determined from the 10C survey (Davies et al. 2011).

There remains the possibility that there exists a population of radio sources that are below our detection threshold and that are correlated with the cluster positions. The extra deep LA pointings that we conducted towards the centres of the clusters were intended to search for, and subsequently account for in our analysis, such a population. Comparing to the sources detected in the shallower LA raster data, these deeper cluster-centred LA observations revealed the presence of fainter sources in six out of the 11 cases. To assess the impact that these further detections have had on our results, we have re-extracted cluster parameters from the observations of these six clusters with the deep LA pointings
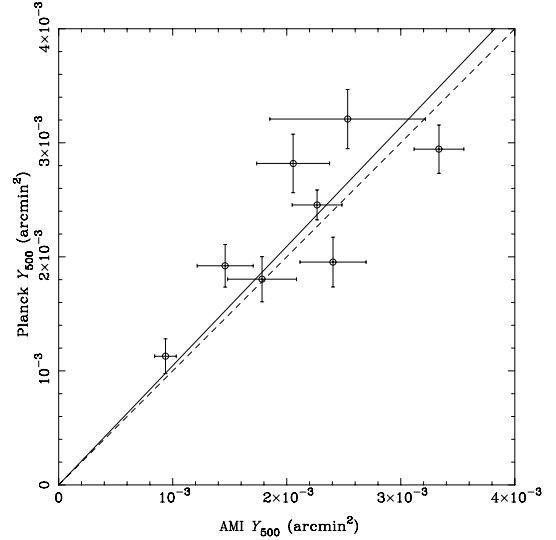

Fig. 6. Comparison of the integrated Compton-*Y* parameters obtained from the *Planck* and AMI fits, when the cluster size is fixed to that determined from X-ray observations. The one-to-one relation is denoted with the dashed line. The best-fitting linear relation is plotted as the unbroken line. The slope of this latter relation is 1.05 ± 0.05 and the correlation coefficient is 0.80. Note that the same general behaviour (slope >1) is also observed when we fix the cluster size to be that determined from either the *Planck* or the AMI SZ observations.

discarded. In all but one case, the derived parameter constraints were negligibly different from those displayed in Fig. 5. The one cluster for which including the newly found fainter sources did significantly impact the results is the case of A1914 where the AMI contours shifted by ~1σ to lower values of Y_{500} when the deep LA data were removed from the analysis. There could, of course, be sources present at even fainter fluxes than those reached by these deep LA observations. However, since they will be fainter still, they are likely to have an even smaller effect on our results than we have found with these tests.

5.3. Results

Figure 5 presents the 2D marginalised posterior distributions in the $Y_{500} - \theta_{500}$ plane and Table 6 summarises the mean and the dispersion of these two parameters for each cluster, as estimated from the *Planck* and AMI data, respectively. Note that in Fig. 5 the inner and outer contours show the areas enclosing 68% and 95% of the probability distributions. Estimates of θ_{500} as derived from X-ray observations, and which were included in the *Planck* ESZ catalogue (Planck Collaboration 2011e), are also indicated in the figures for comparison.

Recall that in this figure the clusters are ordered in terms of increasing redshift. The constraints from both *Planck* and AMI demonstrate a strong cluster size-integrated Compton parameter ($\theta_{500} - Y_{500}$) degeneracy/correlation in all cases. It is important to account for such effects when attempting to use the SZ signal to estimate cluster masses (da Silva et al. 2004; Arnaud et al. 2007). We also note that the *Planck* constraints appear to be weaker for high redshift clusters, which can generally be understood as a resolution effect – *Planck*'s relatively poor resolution (e.g., as compared with AMI) means it has difficulty resolving and thus estimating the parameters of clusters with small angular extent – and high-redshift clusters are likely to be smaller in angular size. AMI's increased resolution, on the other hand, means that it can still constrain the sizes of these high-redshift, small-angular size clusters.
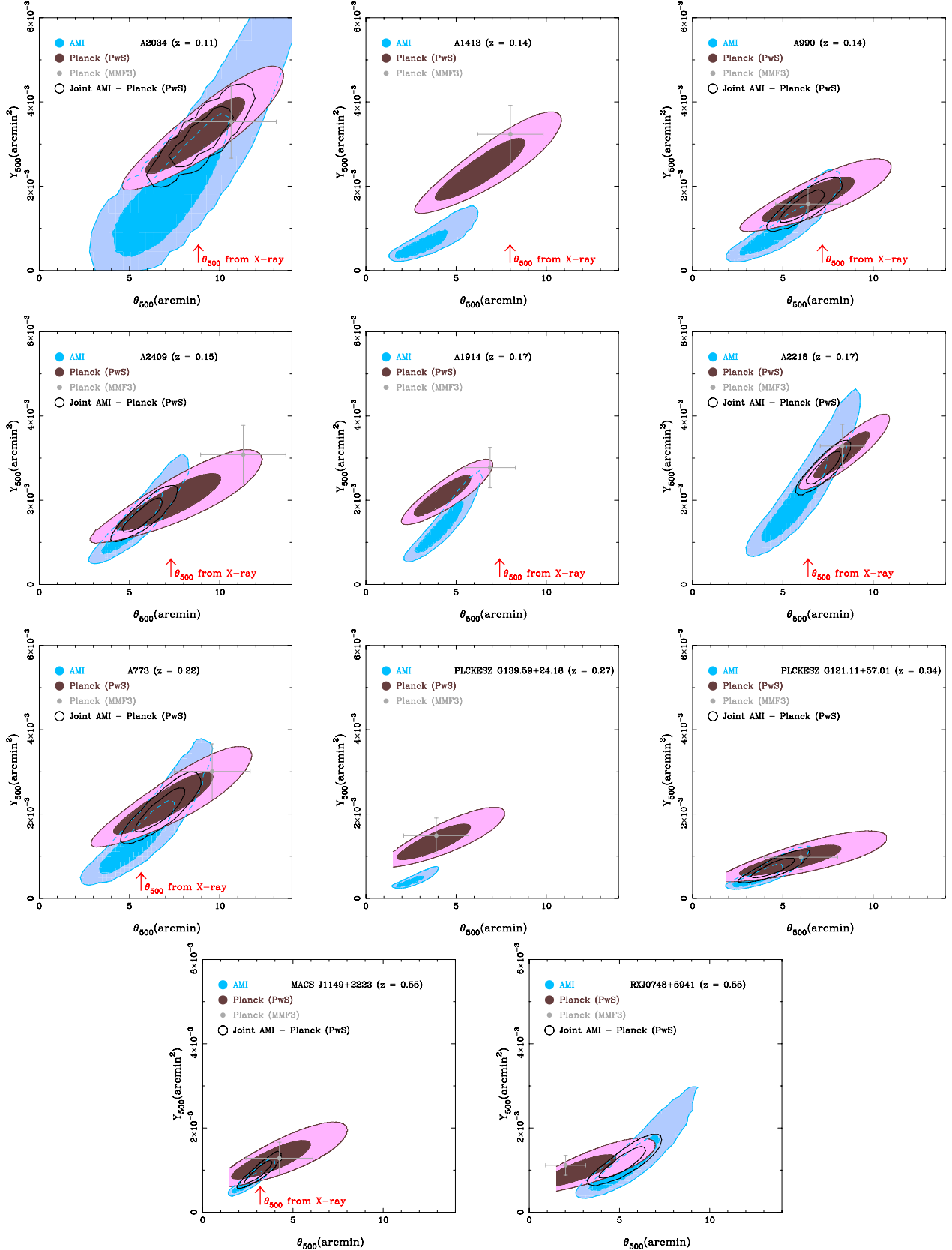
Fig. 5. Recovered *Planck* and AMI 2D posterior distributions in the $Y_{500} - \theta_{500}$ plane. Blue contour plots are the results from the AMI analysis and purple contours show the *Planck* results (specifically using the PwS method). Red arrows show the values of θ_{500} as determined from X-ray measurements of these clusters where available. The grey points with error bars show the MMF3 *Planck* results. The inner and outer contours in each set indicate the areas enclosing 68% and 95% of the probability distribution, while the MMF3 error-bars indicate the 1σ uncertainties. Where the recovered AMI and PwS *Planck* constraints are consistent, the joint constraints are also indicated by the heavy black contours. In cases where the contours do not close at the lower ends of the parameter ranges, the corresponding constraints represent upper limits only.

Table 6. Recovered mean and dispersion values for θ_{500} and Y_{500} for the 11 clusters.

Cluster	z	S/N PwS	*Planck* θ_{500} (arcmin)	*Planck* Y_{500} (10^{-4} arcmin^2)	AMI θ_{500} (arcmin)	AMI Y_{500} (10^{-4} arcmin^2)	Joint θ_{500} (arcmin)	Joint Y_{500} (10^{-4} arcmin^2)
A2034	0.11	13	9.0 ± 1.9	33 ± 6	8.0 ± 2.5	24 ± 14	9.1 ± 1.5	32 ± 4
A1413	0.14	11	6.7 ± 1.7	25 ± 5	3.5 ± 1.1	7 ± 3	$\cdots$	$\cdots$
A990	0.14	10	6.8 ± 1.7	17 ± 4	4.9 ± 1.3	10 ± 4	6.2 ± 0.8	15 ± 2
A2409	0.15	9	7.6 ± 1.9	20 ± 4	5.5 ± 1.2	16 ± 5	5.8 ± 0.8	17 ± 3
A1914	0.17	14	4.4 ± 1.0	21 ± 3	4.3 ± 1.0	14 ± 4	$\cdots$	$\cdots$
A2218	0.17	20	8.4 ± 1.0	31 ± 4	6.0 ± 1.4	22 ± 8	7.3 ± 0.7	28 ± 3
A773	0.22	11	7.3 ± 1.9	23 ± 5	5.8 ± 1.6	16 ± 6	6.8 ± 0.9	21 ± 4
MACS J1149+2223	0.55	8	4.2 ± 1.5	13 ± 3	2.6 ± 0.6	7 ± 2	3.2 ± 0.5	10 ± 2
RXJ0748+5941	0.55	8	3.4 ± 1.4	11 ± 2	5.7 ± 1.4	13 ± 5	5.3 ± 0.9	12 ± 3
PLCKESZ G139.59+24.18	0.27	9	4.2 ± 1.4	14 ± 3	2.6 ± 0.6	4 ± 1	$\cdots$	$\cdots$
PLCKESZ G121.11+57.01	0.34	7	5.9 ± 1.9	9 ± 2	3.9 ± 1.0	6 ± 2	4.6 ± 0.8	7 ± 2

Notes. Where consistency is found between the *Planck* and AMI measurements, the joint constraints are also given. The cluster redshift and signal-to-noise of the PwS detections are also listed.

For three clusters (A1413, A1914, and PLCKESZ G139.59+24.18), the AMI and *Planck* constraints are clearly discrepant. On the other hand there is significant overlap in the posterior distributions for the remaining eight clusters. However, taking our cluster sample as an ensemble, there is some evidence that the cluster parameter estimates derived from the AMI data are systematically lower than those derived from the *Planck* data (i.e., AMI is finding the clusters to be fainter and smaller in angular extent compared to what the *Planck* data indicate).

In addition, the $Y_{500} - \theta_{500}$ degeneracies are significantly different for the *Planck* and AMI constraints, with the degeneracies of the AMI constraints being generally steeper than the *Planck* ones. This arises because of the interplay between the angular size-redshift relation and the differing angular scales that AMI and *Planck* are sensitive to, as well as the very different observational techniques and frequencies used by the two instruments.

In the cases where the *Planck* and AMI-derived constraints are compatible with one another, we also overplot the joint constraints obtained from multiplying the *Planck* and AMI posteriors. In many cases, the resulting joint constraints are far tighter than either analysis alone which is a direct result of the differing parameter degeneracies for the two instruments, as described above. The marginalised constraints from this combined analysis are also presented in Table 6.

In Fig. 5, we have also over-plotted the constraints as obtained from the *Planck* data using the MMF3 algorithm (see Melin et al. 2006, for a detailed description of the MMF3 extraction algorithm). Comparing these results with the PwS *Planck* results, we see good agreement in most cases, although there may be a tendency for the MMF3 estimates to be systematically brighter and larger than the PwS results. However, it is clear that our broad conclusions regarding the general levels of agreement between the *Planck* and AMI results remain unchanged if we consider the MMF3 results in place of the PwS constraints.

In Fig. 6, we plot the *Planck* determined integrated Compton-*Y* parameter versus the Compton-*Y* parameter as derived from the AMI data. Note that, for this correlation plot, we have fixed the cluster scale size to be that determined from X-ray observations (as indicated by the red arrows in Fig. 5). (Three of the clusters have no reported X-ray size so only eight of the 11 clusters contribute to this correlation analysis.) The measured correlation coefficient is 0.80 and the best-fitting linear relationship has a slope of 1.05 ± 0.05, again suggesting that the *Planck* SZ fluxes are systematically larger that the AMI derived

fluxes. We have also repeated this analysis fixing the cluster size to both the *Planck*-determined size and the AMI-determined size. In both cases we see the same general trend, with the *Planck* Compton-*Y* parameter being consistently larger than the AMI-derived value.

In summary, our results suggest a systematic difference between the *Planck* and AMI measurements of the SZ signal coming from our cluster sample. Such a systematic difference could be an indicator of a shortcoming in some part of our analysis and could have important implications for performing cosmological studies with larger samples of SZ clusters. For example, the observed systematic could indicate that the way the clusters are being modeled in the analysis (e.g., the fixed GNFW profile adopted and/or the assumption of spherical symmetry) is not flexible enough to describe both the *Planck* and AMI results simultaneously. If this were to be the source of the discrepancy then such effects would need to be accounted for in future cosmological studies. However, before considering such an explanation, it is important to first consider if possible instrumental and/or astrophysical systematic effects could be responsible for the results we have found. We now turn to simulations to investigate the potential impact of such effects.

6. Simulations

In order to test the SZ signal extraction techniques used and to investigate whether the systematic discrepancy observed in the real data is due to unaccounted-for astrophysical foregrounds, instrumental systematics or data-analysis induced biases, we have conducted simulations of both the *Planck* and AMI experimental setups.

For each of the 11 clusters in our sample, to create an input SZ signal for the simulations, we simulated a cluster SZ signal using the GNFW pressure profile (Eq. (3)), with input parameters based on the best-fitting Y_{500} and θ_{500} values from an analysis based on intermediate *Planck* maps, which are, in practice, close to the best-fitting *Planck* parameters quoted in Table 6. Note that our simulations are limited in the sense that we restrict ourselves to consider only the recovery of parameters from simulated clusters that follow the universal pressure profile. This is the profile assumed for the clusters throughout our analysis of the real data and it is therefore the unbiased recovery of clusters described by this profile that we wish to demonstrate through simulations. Since the assumption of sphericity is implicit in the universal pressure profile parametrisation, we do not consider nonspherical clusters in our simulations. In addition, we

have restricted the signal content of our simulations to include only the thermal SZ effect and have ignored possible kinetic SZ contributions. For the relatively massive clusters which we consider in this paper, we estimate the kinetic contribution to be ~5% based on both hydrodynamical simulations (da Silva et al. 2001a,b) and recent observations (Hand et al. 2012). Thermal-kinetic cross terms are likely to be smaller still. Furthermore, the thermal and kinetic effects would be expected to be randomly aligned amongst the different members of our cluster sample, meaning that exposure to systematic effects due to the kinetic SZ should be diluted still further when the sample is considered as a whole.

6.1. Planck simulations

For *Planck*, the main worry in terms of astrophysical systematics is probably thermal emission from dust in the Galaxy. (See Sect. 6.4 of the Planck ESZ paper (Planck Collaboration 2011e) for an assessment of the various possible astrophysical contaminants of SZ signals extracted from the *Planck* maps.) The *Planck* simulation ensemble comprised of CMB and noise realisations and a fixed foreground dust template, produced by re-scaling the *Planck* 857 GHz channel map to the other HFI frequencies and reconvolving so as to apply the appropriate beam for each channel. The dust template assumed a modified blackbody spectrum with emissivity $\beta = 1.8$ and temperature $T = 18$ K. The beams were assumed to be Gaussian with the appropriate mean FWHM for each channel as calculated by the FEBeCoP algorithm (Planck HFI Core Team 2011b).

The noise component of the simulations was generated using the Springtide destriping pipeline (Ashdown et al. 2007). This pipeline creates realisations of the noise in the nominal mission time-ordered data streams, compresses them to rings and destripes the rings to produce noise maps. It is assumed that the noise is uncorrelated between rings and that in each ring it is drawn from a power spectrum. For these simulations, the noise power spectrum used was the mean of the ring-by-ring spectra. In turn, these were determined by applying the noise estimation pipeline (Planck HFI Core Team 2011b) to the exact same version and time-span of the *Planck* data that was used for the real SZ cluster analysis of the previous section.

The simulations were then analysed using the PwS algorithm in exactly the same manner as was applied during the analysis of the real data. For each of the 11 clusters, ten simulations were run. The dust template based on the *Planck* 857 GHz map was the same for each of these ten simulations, but the CMB and noise realisations were different.

The results of the simulations are shown in Fig. 7. In each panel, input parameters are indicated with a star and the recovered parameter constraints from the ten different simulations are indicated by ten sets of differently coloured contours. Comparing with the input parameters, the recovered constraints for each of our clusters are clearly distributed about the input model and there is no indication of any significant bias due to dust contamination, noise bias, the *Planck* beams or the PwS extraction technique employed.

6.2. AMI simulations

As mentioned in Sect. 4, contamination from radio point sources is a significant issue at AMI frequencies (~16 GHz). Although the AMI LA observations are used to accurately find and model sources in the AMI SA observations, there is the possibility

of contamination from source residuals if this modelling is not perfect.

In a similar manner to the *Planck* simulations described in the previous subsection, we have investigated potential issues associated with either residual foreground radio sources or with the AMI data-analysis methodology and instrument response using simulations. The simulated input clusters were the same as used for the *Planck* simulations.

To simulate the interferometric AMI observations, we used the in-house simulation package, PROFILE (Grainge et al. 2002) to create the mock visibilities. In addition to the cluster signal, the simulations included primordial CMB fluctuations and Gaussian noise, the amplitude of which was chosen to match that measured from the real observations. The simulation package also mimics the actual *uv* coverage and synthesised beam of the real observations. The point sources in each cluster were simulated using the best-fitting values from the analysis of the real data. These simulated observations were then analysed in the exact same way as was used for the real data. Once again, for each of the 11 clusters, ten simulations were performed. Here, the point source environment was kept the same for these ten simulations but the CMB and noise realisations were again different.

The results of the simulations are shown in Fig. 8. In each panel, input parameters are indicated with a star and the recovered parameter constraints from the ten different simulations are indicated by ten sets of differently coloured contours. As was the case with the *Planck* simulations, the recovered constraints for each of our clusters are clearly distributed about the input model. Once again, there is no indication of any significant bias due to residual point source contamination, noise bias, the AMI *uv* coverage and resolution effects, or the extraction technique employed.

7. Adopting individual pressure profiles as measured from X-ray observations

The simulations presented in the previous section indicate that the discrepancies seen in the analysis of the real data cannot be easily explained by astrophysical contamination, instrumental effects, or any issues associated with the SZ signal extraction techniques. It is then interesting to ask whether the discrepancies observed might be associated with the way in which the clusters have been modeled using the universal pressure profile (Arnaud et al. 2010).

For a number of clusters in the sample, we have high-quality determinations of the clusters' individual pressure profiles, as estimated from X-ray observations undertaken with *XMM-Newton*. Rather than adopting the Arnaud et al. (2010) profile (which is essentially an average profile taken over many clusters), one might expect to achieve better consistency on a case-by-case basis if we use these individual best-fitting X-ray derived profiles in the SZ analysis.

We have performed such a re-analysis for five clusters in our sample for which we have high-quality measured *XMM-Newton* X-ray profiles. The clusters concerned are A1413, A1914, A2034, A2218, and A773. We fitted a GNFW pressure profile to the measured X-ray profiles and the results are presented in Table 7. We then re-analysed the *Planck* and AMI SZ data for these five clusters using the best fitting values of the profile shape parameters ($c_{500}, \alpha, \beta, \gamma$) as given in Table 7. The resulting constraints from this re-analysis are shown in Fig. 9.

Comparing with the corresponding constraints for these five clusters in our original analysis, we see that the updated
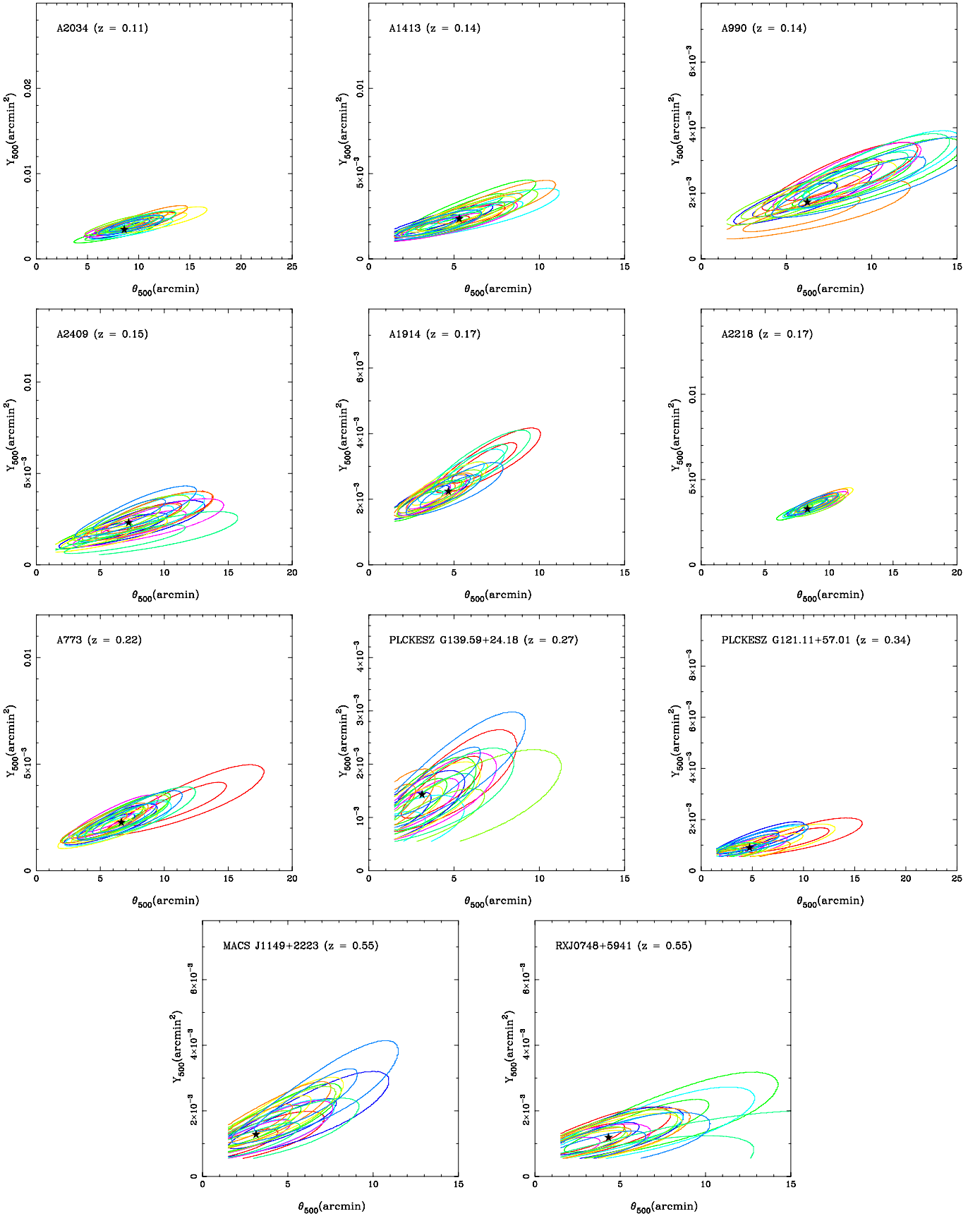
Fig. 7. Recovery of SZ cluster parameters from simulated *Planck* observations (see Sect. 6.1 for details). Each set of recovered parameter constraints (contours with different colours) represents a different realisation of the instrument noise and primordial CMB fluctuations and the star shows the input parameter values. The inner and outer contours in each set indicate the areas enclosing 68% and 95% of the probability distribution. Any bias in the recovery of the input parameters averaged over realisations is negligible compared to the random errors. In cases where the contours do not close at the lower ends of the parameter ranges, the corresponding constraints represent upper limits only.
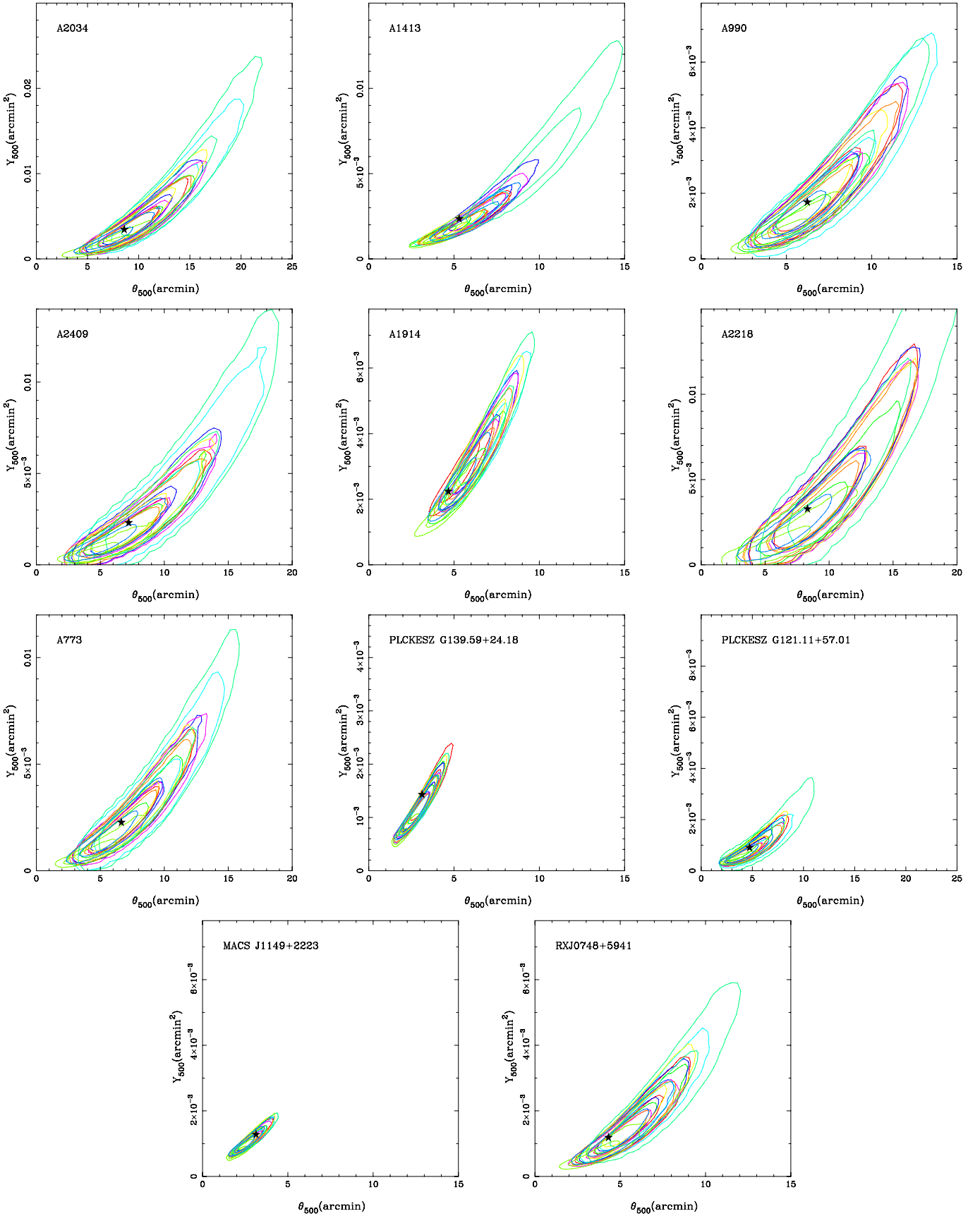
Fig. 8. Recovery of SZ cluster parameters from the simulated AMI observations in the presence of residual point source contamination from imperfectly modeled radio sources for each cluster in the sample. Also included in the simulations are the AMI *uv* coverage, the instrument beams and realisations of the instrument noise and primordial CMB. The different sets of contours indicate different CMB and noise realisations and the star shows the input parameters used to generate the simulated cluster. The inner and outer contours in each set indicate the areas enclosing 68% and 95% of the probability distribution.

Table 7. Best-fitting GNFW shape and concentration parameters (cf. Eq. (3)) derived by fitting the parameterised GNFW profile to the measured X-ray pressure profiles of five clusters in our 11 cluster sample.

Cluster	R_{500} (Mpc)	P_{500}	P_0	c_{500}	α	γ
A1413	1.240	3.229	31.08	0.90	0.69	0.191
A1914	1.348	4.045	49.94	1.88	0.95	0.000
A2034	1.211	2.899	9.14	1.84	1.72	0.000
A2218	1.169	3.039	40.92	1.02	0.74	0.000
A773	1.232	3.724	20.61	1.25	0.96	0.000

Notes. Note that $\beta = 5.49$ is fixed and a prior of $\gamma > 0$ is imposed. This latter constraint is enforced to avoid unphysical pressure gradients being allowed by the GNFW parameterisation.
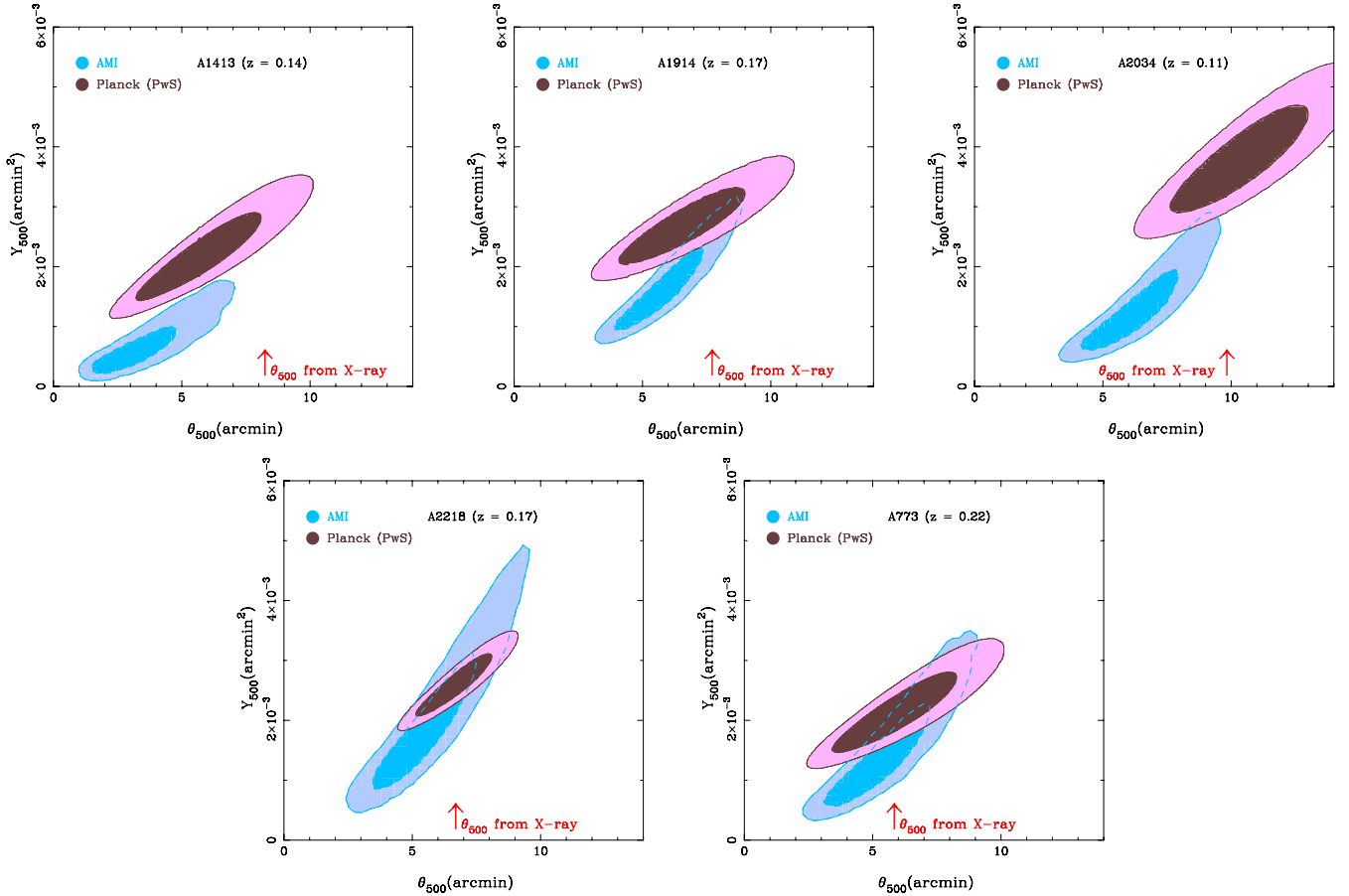
Fig. 9. Constraints obtained from the re-analysis of the *Planck* and AMI observations for the five clusters for which high-quality X-ray observations are available. These re-analyses adopted the GNFW shape parameters which best fit the X-ray data as given in Table 7. Comparison with the corresponding panels in Fig. 5 reveals no obvious improvement in the level of agreement between the *Planck* and AMI constraints. The X-ray sizes indicated here are also derived from the GNFW fits to the high-quality X-ray data. These are slightly different from the X-ray sizes plotted in Fig. 5, which were taken from the ESZ catalogue.

constraints for A2034 have tightened significantly. This appears to be due to the fact that the previously used Arnaud et al. (2010) GNFW profile was not a good match to this particular cluster's pressure profile, particularly in the central region of the cluster, where AMI is sensitive. The GNFW profile variant used to produce the updated constraints is a much better match to the measured X-ray profile and so the AMI data are better able to constrain the remaining cluster parameters.

Apart from this single case, comparing with our original results, there does not appear to be a systematic improvement in the agreement between the *Planck* and AMI constraints when we move from the Arnaud et al. (2010) profile to the best-fitting GNFW profile as measured from the individual X-ray observations. This, and similar reasoning based on an adaptation of these modified profiles to the other clusters in our sample, suggests

that a more significant widening of the parameter space describing the cluster profiles will be required in order to simultaneously fit both the *Planck* and AMI SZ measurements for the entire cluster sample considered in this paper.

8. Conclusions

We have studied the $Y_{500} - \theta_{500}$ degeneracy from the SZ effect for a sample of 11 clusters ($0.11 < z < 0.55$) observed with both *Planck* and AMI. This is motivated by the fact that such a study can potentially break the well-known Y-size degeneracy which commonly results from SZ experiments with limited resolution. Modelling the radial pressure distribution in each cluster using a universal GNFW profile, we have shown that there is significant overlap in the 2D posterior distributions for eight of the clusters.

However, overall, AMI finds the SZ signal to be smaller in angular extent and fainter than *Planck* finds. The derived parameter degeneracies are significantly different for the two instruments. Hence, where the constraints from the two instruments are mutually consistent, their combination can be powerful in terms of reducing the parameter uncertainties. Significant discrepancies are found between the *Planck* and AMI parameter constraints for the remaining three clusters in our sample.

We have investigated the origin of these discrepancies by carrying out a detailed analysis of a series of simulations assessing the potential impact of diffuse thermal emission from dust and residual contamination from imperfectly modeled radio point sources. Our simulations also include a number of systematic effects associated with the two instruments in addition to primordial CMB fluctuations and thermal noise. We find that the results of the simulations of both the *Planck* and AMI analyses are unbiased, confirming the accuracy of the two analysis pipelines and their corresponding methodologies.

We have attempted to reconcile some of the discrepancies seen by re-analysing the *Planck* and AMI data adopting individual best-fitting pressure profiles, as measured from high-quality X-ray observations for five of the clusters in the sample. However, we do not observe a systematic improvement in the agreement between the *Planck* and AMI parameter constraints when we perform this re-analysis.

We conclude that: either (i) there remain unaccounted for systematic effects in one or both of the data sets beyond what are included in our simulations; or (ii) a further expansion of the parameter space used to model the SZ cluster signal is required to simultaneously fit the *Planck* and AMI SZ data. Such further expansion of the model parameter space, which we leave for future studies, could potentially include using the *Planck* and AMI data in conjunction with X-ray observations to find a global fit for the GNFW shape parameters, going beyond the GNFW parameterisation to investigate other cluster profiles, and/or dropping the assumption of spherical symmetry for the SZ (and X-ray) emission.

References

Allison, J. R., Taylor, A. C., Jones, M. E., Rawlings, S., & Kay, S. T. 2011, MNRAS, 410, 341
Andersson, K., Benson, B. A., Ade, P. A. R., et al. 2011, ApJ, 738, 48
Appenzeller, I., Thiering, I., Zickgraf, F.-J., et al. 1998, ApJS, 117, 319
Arnaud, M., Pointecouteau, E., & Pratt, G. W. 2007, A&A, 474, L37
Arnaud, M., Pratt, G. W., Piffaretti, R., et al. 2010, A&A, 517, A92
Ashdown, M. A. J., Baccigalupi, C., Balbi, A., et al. 2007, A&A, 467, 761
Baars, J. W. M., Genzel, R., Pauliny-Toth, I. I. K., & Witzel, A. 1977, A&A, 61, 99
Bartlett, J. G., & Silk, J. 1994, ApJ, 423, 12
Battye, R. A., & Weller, J. 2003, Phys. Rev. D, 68, 083506
Bersanelli, M., Mandolesi, N., Butler, R. C., et al. 2010, A&A, 520, A4
Birkinshaw, M. 1999, Phys. Rep., 310, 97
Böhringer, H., Voges, W., Huchra, J. P., et al. 2000, ApJS, 129, 435
Böhringer, H., Schuecker, P., Pratt, G. W., et al. 2007, A&A, 469, 363
Borgani, S., Murante, G., Springel, V., et al. 2004, MNRAS, 348, 1078

Carlstrom, J. E., Holder, G. P., & Reese, E. D. 2002, ARA&A, 40, 643
Carvalho, P., Rocha, G., & Hobson, M. P. 2009, MNRAS, 393, 681
Carvalho, P., Rocha, G., Hobson, M. P., & Lasenby, A. 2012, MNRAS, 427, 1384
Condon, J. J., & Broderick, J. J. 1985, AJ, 90, 2540
Condon, J. J., & Broderick, J. J. 1986, AJ, 91, 1051
Condon, J. J., Broderick, J. J., & Seielstad, G. A. 1989, AJ, 97, 1064
Crawford, C. S., Edge, A. C., Fabian, A. C., et al. 1995, MNRAS, 274, 75
da Silva, A. C., Barbosa, D., Liddle, A. R., & Thomas, P. A. 2001a, MNRAS, 326, 155
da Silva, A. C., Kay, S. T., Liddle, A. R., et al. 2001b, ApJ, 561, L15
da Silva, A. C., Kay, S. T., Liddle, A. R., & Thomas, P. A. 2004, MNRAS, 348, 1401
Davies, M. L., Franzen, T. M. O., Waldram, E. M., et al. (AMI Consortium) 2011, MNRAS, 415, 2708
Ebeling, H., Edge, A. C., Bohringer, H., et al. 1998, MNRAS, 301, 881
Ebeling, H., Mullis, C. R., & Tully, R. B. 2002, ApJ, 580, 774
Ebeling, H., Barrett, E., Donovan, D., et al. 2007, ApJ, 661, L33
Eriksen, H. K., Banday, A. J., Górski, K. M., & Lilje, P. B. 2004, ApJ, 612, 633
Feroz, F., & Hobson, M. P. 2008, MNRAS, 384, 449
Feroz, F., Hobson, M. P., & Bridges, M. 2009a, MNRAS, 398, 1601
Feroz, F., Hobson, M. P., Zwart, J. T. L., Saunders, R. D. E., & Grainge, K. J. B. 2009b, MNRAS, 398, 2049
Fixsen, D. J. 2009, ApJ, 707, 916
Franzen, T. M. O., Davies, M. L., Waldram, E. M., et al. (AMI Consortium) 2011, MNRAS, 415, 2699
Govoni, F., Murgia, M., Markevitch, M., et al. 2009, A&A, 499, 371
Grainge, K., Jones, M. E., Pooley, G., et al. 2002, MNRAS, 333, 318
Greisen, E. W. 2003, Information Handling in Astronomy – Historical Vistas, 285, 109
Hand, N., Addison, G. E., Aubourg, E., et al. 2012, Phys. Rev. Lett., 109, 041101
Hobson, M. P., & Maisinger, K. 2002, MNRAS, 334, 569
Hurier, G., Hildebrandt, S. R., & Macias-Perez, J. F. 2010 [arXiv:1007.1149]
Hurley-Walker, N., Brown, M. L., Davies, M. L., et al. (AMI Consortium) 2011, MNRAS, 414, L75
Kempner, J. C., Sarazin, C. L., & Markevitch, M. 2003, ApJ, 593, 291
Kneissl, R., Jones, M. E., Saunders, R., et al. 2001, MNRAS, 328, 783
Kocevski, D. D., Ebeling, H., Mullis, C. R., & Tully, R. B. 2007, ApJ, 662, 224
Komatsu, E., Smith, K. M., Dunkley, J., et al. 2011, ApJS, 192, 18
Kosowsky, A. 2003, in APS April Meeting Abstracts, C9015
Kravtsov, A. V., Nagai, D., & Vikhlinin, A. 2005, ApJ, 625, 588
Kravtsov, A. V., Vikhlinin, A., & Nagai, D. 2006, ApJ, 650, 128
Lamarre, J., Puget, J., Ade, P. A. R., et al. 2010, A&A, 520, A9
LaRoque, S. J., Bonamente, M., Carlstrom, J. E., et al. 2006, ApJ, 652, 917
Leahy, J. P., Bersanelli, M., D'Arcangelo, O., et al. 2010, A&A, 520, A8
Mandolesi, N., Bersanelli, M., Butler, R. C., et al. 2010, A&A, 520, A3
Melin, J., Bartlett, J. G., & Delabrouille, J. 2006, A&A, 459, 341
Mennella, A., Butler, R. C., Curto, A., et al. 2011, A&A, 536, A3
Mroczkowski, T., Bonamente, M., Carlstrom, J. E., et al. 2009, ApJ, 694, 1034
Nagai, D. 2006, ApJ, 650, 538
Nagai, D., Kravtsov, A. V., & Vikhlinin, A. 2007, ApJ, 668, 1
Navarro, J. F., Frenk, C. S., & White, S. D. M. 1997, ApJ, 490, 493
Olamaie, M., Rodriguez-Gonzalvez, C., Davies, M. L., et al. (AMI Consortium) 2010 [arXiv:1012.4996]
Patnaik, A. R., Browne, I. W. A., Wilkinson, P. N., & Wrobel, J. M. 1992, MNRAS, 254, 655
Piffaretti, R., & Valdarnini, R. 2008, A&A, 491, 71
Plagge, T., Benson, B. A., Ade, P. A. R., et al. 2010, ApJ, 716, 1118
Planck Collaboration 2011a, A&A, 536, A1
Planck Collaboration 2011b, A&A, 536, A2
Planck Collaboration 2011c, A&A, 536, A9
Planck Collaboration 2011d, A&A, 536, A7
Planck Collaboration 2011e, A&A, 536, A8
Planck Collaboration 2011f, A&A, 536, A10
Planck Collaboration 2011g, A&A, 536, A11
Planck Collaboration 2011h, A&A, 536, A12
Planck Collaboration 2011i, A&A, 536, A26
Planck Collaboration 2012, A&A, 543, A102
Planck HFI Core Team 2011a, A&A, 536, A4
Planck HFI Core Team 2011b, A&A, 536, A6
Pratt, G. W., & Arnaud, M. 2002, A&A, 394, 375
Rodríguez-González, C., Olamaie, M., Davies, M. L., et al. (AMI Consortium) 2011, MNRAS, 414, 3751
Rosset, C., Tristram, M., Ponthieu, N., et al. 2010, A&A, 520, A13
Ruhl, J., Ade, P. A. R., Carlstrom, J. E., et al. 2004, in SPIE Conf. Ser. 5498, eds. C. M. Bradford, P. A. R. Ade, J. E. Aguirre, et al., 11
Sanderson, A. J. R., Ponman, T. J., Finoguenov, A., Lloyd-Davies, E. J., & Markevitch, M. 2003, MNRAS, 340, 989

Shimwell, T. W., Barker, R. W., Biddulph, P., et al. (AMI Consortium) 2012, MNRAS, 423, 1463

Sunyaev, R. A., & Zeldovich, Y. B. 1972, Comments Astrophys. and Space Phys., 4, 173

Tauber, J. A., Mandolesi, N., Puget, J., et al. 2010, A&A, 520, A1

Vikhlinin, A., Markevitch, M., Murray, S. S., et al. 2005, ApJ, 628, 655

Vikhlinin, A., Kravtsov, A., Forman, W., et al. 2006, ApJ, 640, 691

Waldram, E. M., Pooley, G. G., Grainge, K. J. B., et al. 2003, MNRAS, 342, 915

White, R. L., & Becker, R. H. 1992, ApJS, 79, 331

White, S. D. M., Navarro, J. F., Evrard, A. E., & Frenk, C. S. 1993, Nature, 366, 429

Zacchei, A., Maino, D., Baccigalupi, C., et al. 2011, A&A, 536, A5

Zwart, J. T. L., Barker, R. W., Biddulph, P., et al. (AMI Consortium) 2008, MNRAS, 391, 1545

Zwart, J. T. L., Feroz, F., Davies, M. L., et al. (AMI Consortium) 2011, MNRAS, 418, 2754

[1] APC, AstroParticule et Cosmologie, Université Paris Diderot, CNRS/IN2P3, CEA/lrfu, Observatoire de Paris, Sorbonne Paris Cité, 10 rue Alice Domon et Léonie Duquet, 75205 Paris Cedex 13, France

[2] Aalto University Metsähovi Radio Observatory, Metsähovintie 114, 02540 Kylmälä, Finland

[3] Academy of Sciences of Tatarstan, Bauman Str., 20, Kazan, 420111 Republic of Tatarstan, Russia

[4] Agenzia Spaziale Italiana Science Data Center, c/o ESRIN, via Galileo Galilei, Frascati, Italy

[5] Agenzia Spaziale Italiana, Viale Liegi 26, Roma, Italy

[6] Astrophysics Group, Cavendish Laboratory, University of Cambridge, J J Thomson Avenue, Cambridge CB3 0HE, UK

[7] Atacama Large Millimeter/submillimeter Array, ALMA Santiago Central Offices, Alonso de Cordova 3107, Vitacura, Casilla 763 0355, Santiago, Chile

[8] CITA, University of Toronto, 60 St. George St., Toronto, ON M5S 3H8, Canada

[9] CNRS, IRAP, 9 Av. colonel Roche, BP 44346, 31028 Toulouse Cedex 4, France

[10] California Institute of Technology, Pasadena, California, USA

[11] Centre of Mathematics for Applications, University of Oslo, Blindern, Oslo, Norway

[12] Centro de Astrofísica, Universidade do Porto, Rua das Estrelas, 4150-762 Porto, Portugal

[13] Centro de Estudios de Física del Cosmos de Aragón (CEFCA), Plaza San Juan, 1, planta 2, 44001 Teruel, Spain

[14] Computational Cosmology Center, Lawrence Berkeley National Laboratory, Berkeley, California, USA

[15] Consejo Superior de Investigaciones Científicas (CSIC), Madrid, Spain

[16] DSM/Irfu/SPP, CEA-Saclay, 91191 Gif-sur-Yvette Cedex, France

[17] DTU Space, National Space Institute, Technical University of Denmark, Elektrovej 327, 2800 Kgs. Lyngby, Denmark

[18] Département de Physique Théorique, Université de Genève, 24, Quai E. Ansermet, 1211 Genève 4, Switzerland

[19] Departamento de Física, Universidad de Oviedo, Avda. Calvo Sotelo s/n, Oviedo, Spain

[20] Department of Astronomy and Geodesy, Kazan Federal University, Kremlevskaya Str., 18, 420008 Kazan, Russia

[21] Department of Astrophysics, IMAPP, Radboud University, PO Box 9010, 6500 GL Nijmegen, The Netherlands

[22] Department of Physics & Astronomy, University of British Columbia, 6224 Agricultural Road, Vancouver, British Columbia, Canada

[23] Department of Physics and Astronomy, Dana and David Dornsife College of Letter, Arts and Sciences, University of Southern California, Los Angeles, CA 90089, USA

[24] Department of Physics and Astronomy, University of Sussex, Brighton BN1 9QH, UK

[25] Department of Physics, Gustaf Hällströmin katu 2a, University of Helsinki, Helsinki, Finland

[26] Department of Physics, University of California, Berkeley, California, USA

[27] Department of Physics, University of California, Santa Barbara, California, USA

[28] Department of Physics, University of Illinois at Urbana-Champaign, 1110 West Green Street, Urbana, Illinois, USA

[29] Department of Statistics, Purdue University, 250 N. University Street, West Lafayette, Indiana, USA

[30] Dipartimento di Fisica e Astronomia G. Galilei, Università degli Studi di Padova, via Marzolo 8, 35131 Padova, Italy

[31] Dipartimento di Fisica, Università La Sapienza, P. le A. Moro 2, Roma, Italy

[32] Dipartimento di Fisica, Università degli Studi di Milano, via Celoria, 16, Milano, Italy

[33] Dipartimento di Fisica, Università degli Studi di Trieste, via A. Valerio 2, Trieste, Italy

[34] Dipartimento di Fisica, Università di Ferrara, via Saragat 1, 44122 Ferrara, Italy

[35] Dipartimento di Fisica, Università di Roma Tor Vergata, via della Ricerca Scientifica, 1 Roma, Italy

[36] Dipartimento di Matematica, Università di Roma Tor Vergata, via della Ricerca Scientifica 1, Roma, Italy

[37] Discovery Center, Niels Bohr Institute, Blegdamsvej 17, Copenhagen, Denmark

[38] Dpto. Astrofísica, Universidad de La Laguna (ULL), 38206 La Laguna, Tenerife, Spain

[39] European Southern Observatory, ESO Vitacura, Alonso de Cordova 3107, Vitacura, Casilla 19001, Santiago, Chile

[40] European Space Agency, ESAC, Planck Science Office, Camino bajo del Castillo, s/n, Urbanización Villafranca del Castillo, Villanueva de la Cañada, Madrid, Spain

[41] European Space Agency, ESTEC, Keplerlaan 1, 2201 AZ Noordwijk, The Netherlands

[42] Helsinki Institute of Physics, Gustaf Hällströmin katu 2, University of Helsinki, Helsinki, Finland

[43] INAF – Osservatorio Astronomico di Padova, Vicolo dell'Osservatorio 5, Padova, Italy

[44] INAF – Osservatorio Astronomico di Roma, via di Frascati 33, Monte Porzio Catone, Italy

[45] INAF – Osservatorio Astronomico di Trieste, via G.B. Tiepolo 11, Trieste, Italy

[46] INAF Istituto di Radioastronomia, via P. Gobetti 101, 40129 Bologna, Italy

[47] INAF/IASF Bologna, via Gobetti 101, Bologna, Italy

[48] INAF/IASF Milano, via E. Bassini 15, Milano, Italy

[49] INFN, Sezione di Roma 1, Università di Roma Sapienza, Piazzale Aldo Moro 2, 00185 Roma, Italy

[50] INRIA, Laboratoire de Recherche en Informatique, Université Paris-Sud 11, Bâtiment 490, 91405 Orsay Cedex, France

[51] IUCAA, Post Bag 4, Ganeshkhind, Pune University Campus, 411 007 Pune, India

[52] Imperial College London, Astrophysics group, Blackett Laboratory, Prince Consort Road, London, SW7 2AZ, UK

[53] Infrared Processing and Analysis Center, California Institute of Technology, Pasadena, CA 91125, USA

[54] Institut Néel, CNRS, Université Joseph Fourier Grenoble I, 25 rue des Martyrs, Grenoble, France

[55] Institut Universitaire de France, 103 bd Saint-Michel, 75005 Paris, France

[56] Institut d'Astrophysique Spatiale, CNRS UMR8617 Université Paris-Sud 11, Bâtiment 121, Orsay, France

[57] Institut d'Astrophysique de Paris, CNRS UMR7095, 98 bis boulevard Arago, 75014 Paris, France

[58] Institut de Ciències de l'Espai, CSIC/IEEC, Facultat de Ciències, Campus UAB, Torre C5 par-2, 08193 Bellaterra, Spain

[59] Institute for Space Sciences, Bucharest-Magurale, Romania

[60] Institute of Astro and Particle Physics, Technikerstrasse 25/8, University of Innsbruck, 6020 Innsbruck, Austria

[61] Institute of Astronomy and Astrophysics, Academia Sinica, Taipei, Taiwan

[62] Institute of Astronomy, University of Cambridge, Madingley Road, Cambridge CB3 0HA, UK

[63] Institute of Theoretical Astrophysics, University of Oslo, Blindern, Oslo, Norway

[64] Instituto de Astrofísica de Canarias, C/vía Láctea s/n, La Laguna, Tenerife, Spain

[65] Instituto de Física de Cantabria, CSIC-Universidad de Cantabria, Avda. de los Castros s/n, Santander, Spain

[66] Istituto di Fisica del Plasma, CNR-ENEA-EURATOM Association, via R. Cozzi 53, Milano, Italy

[67] Jet Propulsion Laboratory, California Institute of Technology, 4800 Oak Grove Drive, Pasadena, California, USA

[68] Jodrell Bank Centre for Astrophysics, Alan Turing Building, School of Physics and Astronomy, The University of Manchester, Oxford Road, Manchester, M13 9PL, UK

[69] Kavli Institute for Cosmology Cambridge, Madingley Road, Cambridge, CB3 0HA, UK

[70] LAL, Université Paris-Sud, CNRS/IN2P3, Orsay, France

[71] LERMA, CNRS, Observatoire de Paris, 61 Avenue de l'Observatoire, Paris, France

[72] Laboratoire AIM, IRFU/Service d'Astrophysique – CEA/DSM – CNRS – Université Paris Diderot, Bât. 709, CEA-Saclay, 91191 Gif-sur-Yvette Cedex, France

[73] Laboratoire de Physique Subatomique et de Cosmologie, Université Joseph Fourier Grenoble I, CNRS/IN2P3, Institut National Polytechnique de Grenoble, 53 rue des Martyrs, 38026 Grenoble Cedex, France

[74] Laboratoire de Physique Théorique, Université Paris-Sud 11 & CNRS, Bâtiment 210, 91405 Orsay, France

[75] Lawrence Berkeley National Laboratory, Berkeley, California, USA

[76] Max-Planck-Institut für Astrophysik, Karl-Schwarzschild-Str. 1, 85741 Garching, Germany

[77] Max-Planck-Institut für Extraterrestrische Physik, Giessenbachstraße, 85748 Garching, Germany

[78] Niels Bohr Institute, Blegdamsvej 17, Copenhagen, Denmark

[79] Observational Cosmology, Mail Stop 367-17, California Institute of Technology, Pasadena, CA, 91125, USA

[80] Optical Science Laboratory, University College London, Gower Street, London, UK

[81] SISSA, Astrophysics Sector, via Bonomea 265, 34136 Trieste, Italy

[82] School of Physics and Astronomy, Cardiff University, Queens Buildings, The Parade, Cardiff, CF24 3AA, UK

[83] Space Research Institute (IKI), Profsoyuznaya 84/32, Moscow, Russia

[84] Space Research Institute (IKI), Russian Academy of Sciences, Profsoyuznaya Str, 84/32, 117997 Moscow, Russia

[85] Space Sciences Laboratory, University of California, Berkeley, California, USA

[86] Special Astrophysical Observatory, Russian Academy of Sciences, Nizhnij Arkhyz, Zelenchukskiy region, 369167 Karachai-Cherkessian Republic, Russia

[87] Stanford University, Dept of Physics, Varian Physics Bldg, 382 via Pueblo Mall, Stanford, California, USA

[88] Tübitak National Observatory, Akdeniz University Campus, 07058 Antalya, Turkey

[89] UPMC Univ. Paris 6, UMR 7095, 98bis boulevard Arago, 75014 Paris, France

[90] Université de Toulouse, UPS-OMP, IRAP, 31028 Toulouse, Cedex 4, France

[91] University Observatory, Ludwig Maximilian University of Munich, Scheinerstrasse 1, 81679 Munich, Germany

[92] University of Granada, Departamento de Física Teórica y del Cosmos, Facultad de Ciencias, Granada, Spain

[93] University of Miami, Knight Physics Building, 1320 Campo Sano Dr., Coral Gables, Florida, USA

[94] Warsaw University Observatory, Aleje Ujazdowskie 4, 00-478 Warszawa, Poland